TOWARD A SIMULATION FRAMEWORK FOR MAGNETIC RESONANCE FINGERPRINTING (MRF) USING SPIRAL UNDERSAMPLING

By

Muhammed Erziku

In Partial Fulfillment of the Requirements for the Degree of Master of Science in Biomedical Engineering

Center of Biomedical Engineering
Addis Ababa Institute of Technology
Addis Ababa University

Advisor/s: Dr. Dawit Assefa Haile (PhD)

December 2020

Addis Ababa, Ethiopia

Declaration

I, the undersigned, declare that this thesis is my original work. It has never presented for a degree in any other institution and all sources of materials used in it have been properly acknowledged.

Name: __________________________
Signature: __________________________
Date: _____________________________

This MSc. Thesis has been submitted for examination with my approval as an advisor.

____
Dr. Dawit Assefa Haile

Certificate of Examination

This is to confirm that the thesis prepared by Muhammed Erziku entitled "**Toward A Simulation Framework For Magnetic Resonance Fingerprinting Using Spiral Undersampling"** submitted in partial fulfillment of the requirements for the degree of Master of Science in Biomedical Engineering (Bioinstrumentation and Imaging) act in accordance with the regulation of the university and meets the accepted standards with respect to originality and quality.

Signed by the examining committee

Examiner __________________________signature_______________data_____________

Examiner __________________________signature_______________data_____________

Advisor __________________________ signature_______________data_____________

____

Chief of Department or Graduate Program Coordinator

Acknowledgments

I would want to show my gratitude to my supervisor, Dr. Dawit Assefa, for all the valuable feedback on this work. Thank you very much for sharing your knowledge in this field with me.

Dr. AbdEl-Monem El-Sharkawy is acknowledged for his mentorship during my visiting period at Cairo University as a visiting research student.

Finally, I would like to extend my sincere gratefulness to the project hold under the African Biomedical Engineering Mobility (ABEM) project which is funded by the Intra-Africa Academic Mobility Scheme of the Education, Audiovisual and Culture Executive Agency (EACEA) of the European Commission.

Thank you all so much once again!

Dedication

I dedicate this work to my family.

Table of Contents

List of Tables

List of Figures

Acronyms

MRF	Magnetic Resonance Fingerprinting
MRI	Magnetic Resonance Imaging
QMRI	Quantitative Magnetic Resonance Imaging
NUFFT	Non-Uniform Fast Fourier Transform
PD	Proton Density
DF	Off-Resonance
IR_BSSFP	Inversion Recovery Balanced Steady-state Free Precision
FFT	Fast Fourier Transform
DESPOT1	Driven Equilibrium Single Pulse Observation of T1
DESPOT2	Driven Equilibrium Single Pulse Observation of T2
ROI	Region of Interest
R	Undersampling Factor
STD	Standard Deviation
VDS	Variable Density Sampling
FA	Flip Angle
TR	Reptation Time

Abstract

Magnetic Resonance (MR) is a powerful and multipurpose measurement technique to look inside the human body using magnetic properties of the body non-invasively. Quantification of tissue properties including the relaxation parameters has long been a goal of magnetic resonance imaging (MRI), to provide a basis for diagnosis, longitudinal study and, inter-patient comparability. However, prolonged acquisition times have hindered the usage of quantification for clinical applications. Magnetic Resonance Fingerprinting (MRF) was introduced as a promising technique for simultaneous and fast quantification of multiple tissue parameters through a new approach to data acquisition and postprocessing. However, the development and optimization of MRF process is time-consuming, expensive which requisite repetitive experiment and often needs a synthetic phantom or human subject to test it on the real scanner and detect the results. This work aimed to develop an implementation of a Simulation Framework for MRF based on spiral under-sampling. Simulation framework for magnetic resonance fingerprinting (MRF) along with evaluating the effect of noise on the parameter map is significantly studied by using custom generated phantom and phantom generated from the brain web of a simulated database. The undersampling capability of MRF is significantly studied and evaluated by comparing the parameter map that is generated at each undersampling level. Significant undersampling is used to make the MRF time-efficient with several undersampling folds and undersampling with the factor of 24-fold is substantially evaluated and results in acceptable tissue quantification result irrespective of the undersampling artifacts. A comparison between the proposed MRF simulation and the existing simulation used for MRF was done and the proposed methods showed superior results to simulate the effect of gradient on the reconstructed image and at the quantified parameter map. The effect of noise on the parameter map is evaluated by adding different levels of noise on the simulated kspace signal. At a given undersampling level, as the level of noise increases, its effect on the parameter maps gets more and more pronounced specifically in the off-resonance map.

Chapter 1 : **Introduction**

1.1. Magnetic Resonance imaging

Magnetic resonance imaging (MRI) has become one of the most popular imaging modalities in health care due to its excellent soft-tissue contrast without employing ionizing radiation which is very harmful to humans. Nowadays different modalities are used for medical imaging including X-ray, Ultrasound, Computed Tomography (CT), and MRI. These modalities are used in the health care delivery system and medical research areas to provide anatomical, morphological, and functional information from the human body non-invasively. Some of the applications include disease diagnosis, treatment monitoring, and guidance.

Various physical and psychological tissue properties like MR specific parameters including longitudinal relaxation time (or spin-lattice relaxation time T1), transverse relaxation time (or spin-spin relaxation time T2), perfusion, and diffusion can be sensitized by using MRI [1, 2]. These parameters demonstrate different aspects of the tissue properties, which could potentially be more sensitive and specific to a disease status compared to images from other kinds of imaging modalities.

In spite of this, MRI scanning is time-consuming which makes it more sensitive to motion artifacts and inappropriate for quick scanning. Clinical MRI uses qualitative or weighted measurements and the quantification of underlying physical parameters is infrequently performed. Quantitative MRI (QMRI) has the potential to be more informative than conventional MRI because conventional MRI is qualitative and provides images composed of pixels (in two-dimensional imaging) that are informative only relative to each other, not individually [3, 4]. As such the same subject measured with a qualitative sequence with various coils or on different MRI scanners can lead to intensity variations depending on the scanner setup, which limits comparison between different scans [5].

Since its origin, MRI has improved significantly in imaging quality and speed. This has revolutionized diagnostic medicine. Imaging speed is a major part of this development and is essential in many MRI applications. One struggle to improve imaging speed focused on faster data collection. This has been mainly realized by enhancements in MRI hardware, development of fast pulse sequences, and efficient scanning trajectories.

MR fingerprinting (MRF) [5] is a novel quantitative technique that has shown great potential to simultaneously and efficiently obtain multiple parameter maps including T1, T2, Off-resonance, and

PD. Unlike other qMRI techniques, MRF is fast and it can detect more than one parameter at a time which will save. MRF has three major components. The first step is acquiring a dataset with randomized repetition times (TRs) and flip angles (FAs). Then a dictionary containing signal evolution of relevant T1, Off-resonance, and T2 values is constructed. Finally, there is a dictionary matching process where parameter maps are generated by a pixel-wise pattern matching between the acquired data and the dictionary

Simulation framework as an alternative to real-life experiments has several aids and has been used since the development of MRI. Complex systems and physical phenomena can be studied under ideal/perfect and fully controlled conditions without the need for expensive materials [6, 7].

The overall goal of the current thesis is to develop and validate a simulation framework for MR Fingerprinting (MRF) using spiral trajectory as a sampling technique. Specifically, the thesis describes the concept of MRF using a simulation framework with a spiral under-sampling scheme that provides a quantitative measurement of multiple tissue properties with the evaluation of spiral under sampling effect on Inversion Recovery Balanced Steady-State Free Precision (IR_BSSFP) MRF parameter map and effect of noise on MRF.

1.2. Background

1.2.1. Magnetization

The sensation of magnetic resonance emanates from atoms with an odd number of protons and/or neutrons. These atoms have a fundamental quantum property of spin angular momentum, simply referred to as spin, resulting in possession of magnetic dipole moment μ. Magnetic dipole moments are randomly distributed without applying an external magnetic field. In the presence of an external magnetic field **B**, the magnetic dipole moments are aligned in the direction of **B** producing a non-zero net magnetization **M**. The magnetization is referred to as the sum of the magnetic dipole moments over a unit volume [2].

1.2.2. Precession

When the magnetization is in the external magnetic field, the behavior of the magnetization is well-defined by the equation:

$$\frac{dM}{dt} = M\gamma \times B \qquad [1.1]$$

where γ is the gyromagnetic ratio. The gyromagnetic ratio is a unique constant for different atoms. For the case of 1H (Hydrogen), which is the main signal source of MRI because of its abundance in the human body (mostly in H2O), the gyromagnetic ratio is 42.577 MHz/T [2]. Equation 1.1 tells that when the magnetizations are off the direction of the main magnetic field B0, which is the longitudinal axis and commonly chosen to be the z-axis, the precession about B0 is induced at a specific frequency called the Larmor frequency ω or f:

$$\omega = \gamma B0 \left(\frac{rad}{s}\right) \quad [1.2]$$

$$f = \gamma 2\pi B0 \,(Hz) \quad [1.3]$$

where B0 is the strength of the main magnetic field.

1.2.3. Excitation

To nutate the magnetization at its equilibrium alignment, a radiofrequency (RF) magnetic field **B1** rotating at the Larmor frequency must be applied in the transverse plane (commonly chosen to be xy-plane). The magnetization is resonant with **B1** and nutates further away from the longitudinal axis. The behavior of the magnetization is depicted in Fig. 1 below [2]. To simply describe the behavior of the magnetization, a rotating frame is introduced which rotates in clockwise at the Larmor frequency about the longitudinal axis. In the rotating frame, the magnetization moves as if **B1** is the only effective magnetic field present. The angle between the magnetization and the longitudinal axis is defined as a flip angle. It is determined by the strength and the duration of the applied RF field. The transverse component of the magnetization Mxy is detected by the receive coil via Faraday's law of induction.

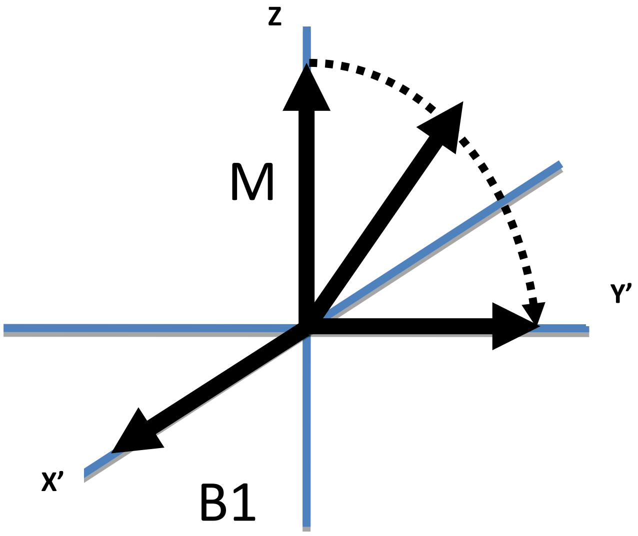

Figure 1: The excitation process in the rotating frame.

1.2.4. Relaxation

Once the magnetization is excited using RF, it returns to the initial equilibrium state by exchanging energy and interacting with the environment through the process called relaxation which can be described by its longitudinal and transverse components [2].

T1 relaxation or the longitudinal relaxation refers to the growth of the longitudinal magnetization (Mz) to the initial state (M0) according to:

$$\frac{d\boldsymbol{M_z}}{d\boldsymbol{t}} = \frac{\boldsymbol{M_0} - \boldsymbol{M_z}}{\boldsymbol{T_1}} \qquad [\mathbf{1}.4]$$

$$\boldsymbol{M_z}(\boldsymbol{t}) = \boldsymbol{M_0} + (\boldsymbol{M_z}(\boldsymbol{0}) - \boldsymbol{M_0})\boldsymbol{e}^{-\boldsymbol{t}/\boldsymbol{T_1}} \qquad [\mathbf{1}.5]$$

where T1 is the spin-lattice relaxation time, which describes the interaction between spin system and the lattice of the object. T1 relaxation arises from the energy exchanges of spins with their neighboring nuclei or atoms.

T2 relaxation or the transverse relaxation refers to the decay of the transverse magnetization (Mxy) according to:

$$\frac{d\boldsymbol{M_{xy}}}{d\boldsymbol{t}} = -\frac{\boldsymbol{M_{xy}}}{\boldsymbol{T_2}} \qquad [\mathbf{1}.6]$$

$$\boldsymbol{M_{xy}}(\boldsymbol{t}) = \boldsymbol{M_0}\boldsymbol{e}^{-\boldsymbol{t}/\boldsymbol{T_2}} \qquad [\mathbf{1}.7]$$

where T2 is the spin-spin relaxation, which describes the interactions between spins with slightly different precession frequency. Therefore, MR signal in terms of relaxation effects can be characterized by exponential equations with respect to relaxation times T1 and T2.

1.2.5. Bloch Equation

Merging the precessional behavior and the relaxation process, the dynamics of the magnetization [2, 8] is described by the Bloch equation as follows:

$$\frac{d\boldsymbol{M}}{d\boldsymbol{t}} = \boldsymbol{M} \times \boldsymbol{\gamma B} - \frac{\boldsymbol{M_{xi}} + \boldsymbol{M_{yj}}}{\boldsymbol{T_2}} - \frac{(\boldsymbol{M_z} - \boldsymbol{M_0})\boldsymbol{k}}{\boldsymbol{T_1}} \qquad [\mathbf{1}.8]$$

where **i, j, k** are the unit vectors representing x, y, z directions respectively. The Bloch equation can be expressed in matrix form as:

$$\boldsymbol{\frac{d}{dt}\begin{bmatrix} M_x \\ M_y \\ M_z \end{bmatrix} = \begin{bmatrix} \frac{-1}{T_2} & \gamma B_z & \gamma B_y \\ -\gamma B_z & \frac{-1}{T_2} & \gamma B_x \\ \gamma B_z & -\gamma B_x & \frac{-1}{T_1} \end{bmatrix} \begin{bmatrix} M_x \\ M_y \\ M_z \end{bmatrix} + \begin{bmatrix} 0 \\ 0 \\ \frac{M_0}{T_1} \end{bmatrix}} \qquad [\mathbf{1}.9]$$

The solution of the above differential equation is given by:

$$\boldsymbol{\begin{bmatrix} M_x \\ M_y \\ M_z \end{bmatrix} = \begin{bmatrix} E_2 cos(\varphi) & -E_2 cos(\varphi) & 0 \\ E_2 sin(\varphi) & E_2 cos(\varphi) & 0 \\ 0 & 0 & E_1 \end{bmatrix} \begin{bmatrix} M_x \\ M_y \\ M_z \end{bmatrix} + \begin{bmatrix} 0 \\ 0 \\ (1 - E_1) M_0 \end{bmatrix}} \qquad [\mathbf{1}.10]$$

where $E_1 = e^{-t/T_1}$, $E_2 = e^{-t/T_2}$ and $\varphi = 2\pi\Delta\omega$

1.3. Principles of Magnetic Resonance Imaging

1.3.1. Kspace

Once the spins within a slice are excited, the spins distributed everywhere in the plane must be differentiated to form a 2D image. It is a phenomenal thing that the image can be obtained by Fourier transforming the signals manipulated by the MRI. Fourier transform is a mathematical operation that decomposes a temporal signal into the frequency components that constitute the signal. Likewise, a 2D image can be decomposed into a 2D set of spatial frequencies by 2D Fourier transform. The spatial frequency domain is brought up as k-space [1]. The gradient coils in MRI produce linearly varying magnetic field strength. Then the resonance frequencies also linearly vary. Let's say the gradient field is applied along the y direction, for simplicity, then the resonance frequency at location y becomes:

$$\omega(y) = \gamma\left(B_0 + G_y y\right) = \gamma B_0 + \gamma G_y y \qquad [1.11]$$

where G_y denotes the gradient fields along the y-direction. When the magnetization is considered in the rotating frame, the Larmor frequency $\gamma B0$ can be neglected. If the gradient waveform is a function of time, $G_y(t)$, then the phase accumulated during time t becomes:

$$\phi(y,t) = \int_0^t \gamma G_y(\tau)\, y d\tau \qquad [1.12]$$

As the time the gradient field is applied increases, the phase spreads out more across the object. The spatial frequency k is defined as the amount of phase spread, the phase cycles per unit distance:

$$\boldsymbol{K_y(t) = \frac{\gamma}{2\pi}\int_0^t G_y(\tau)d\tau} \qquad [\mathbf{1.}13]$$

Gradient fields applied for the appropriate time create phase distributions corresponding to the spatial frequencies. Since the received MR signal itself is the Fourier-encoded signal of the object at some spatial frequency, acquiring MR signal is equivalent to the process that fills in the *k*-space matrix by controlling the strength and/or the duration of the gradient fields.

The received signal is the sum of all precessing magnetization vectors. The 2D encoded signal can be written as [9]:

$$\boldsymbol{S\left(K_x(t), K_y(t)\right) = \iint \rho(x, y, z_0)\, e^{-i2\pi(K_x(t)x + K_y(t)y)} dxdy} \qquad [\mathbf{1.}14]$$

with z_0 the position of the slice selection, $\rho(x, y, z_0)$ the density of the magnetization vector

$$\boldsymbol{K_x(t) = \tfrac{\gamma}{2\pi}\int_0^t G_x(\tau)d\tau} \qquad \textbf{and} \qquad \boldsymbol{K_y(t) = \tfrac{\gamma}{2\pi}\int_0^t G_y(\tau)d\tau} \qquad \textbf{[1.15]}$$

1.3.2. Sampling Trajectory

There is a significant choice in designing the *k*-space trajectory for each acquisition. Most pulse sequences used in clinical imaging today are Cartesian. Reconstruction from such acquisitions is simple by applying the inverse Fast Fourier Transform (FFT). More importantly, reconstructions from Cartesian sampling are robust to many sources of system imperfections. Even though Cartesian trajectories are by far the most popular, many other trajectories are in use, including sampling along radial lines and sampling using spiral trajectories. Radial acquisitions are less susceptible to motion artifacts than Cartesian trajectories [10], and can be significantly under-sampled [11]. Spirals make efficient use of the gradient system hardware, and are used in real-time and rapid imaging applications [12, 13, 14, 15, 16]. Reconstruction from such non-Cartesian trajectories is more complicated, requiring *k*-space interpolation schemes (e.g., gridding [17]) and density compensation methods [16, 18].

1.3.3. Non -Cartesian Image Reconstruction

It can be observed immediately from Eqn. 1.14 that this signal equation is in the form of a two-dimensional Fourier transform, which means that the underlying spin density will be reconstructed with direct use of an inverse Fourier transform on the signal. The sampling positions K_y and K_x are defined by the k-space trajectory since it is assumed that data points are sampled equidistantly and on a Cartesian grid. While this assumption is valid in the case of a conventional Cartesian sampling pattern. But in non-Cartesian sampling, data points have to be interpolated to a Cartesian grid before inverse Fourier transform is applied. The sampled non-Cartesian data has to be convolved with the re-gridding kernel. To interpolate the data points on a rectangular grid, the results of this convolution are evaluated at n × n grid points with a spacing Δk. An optimal kernel window for interpolation in k-space is an infinite sinc function because the corresponding multiplication with a rectangular function does not distort the reconstructed image. However, as a convolution with an infinite kernel window is not feasible in practice, a kernel with compact support has to be used. A systematic assessment of the performance of different kernel windows can be found in different literatures [19, 17]. For simplicity of notation, the following description of the gridding algorithm is restricted to the 1D case.

If the regridded Cartesian k-space data is denoted by $R_C(k)$, the original non-Cartesian data by $W(kj)$, and $C(k)$ is the convolution kernel, this operation can be written as:

$$\boldsymbol{R_C(k) = \sum_j W(kj).C(k-kj) = W(kj) * C(k)} \qquad [\mathbf{1}.16]$$

where k is the k-space index on the Cartesian grid (kx, ky in the 2D case) and kj denotes an arbitrary (not equidistantly sampled and not on a Cartesian grid) k-space position. Please note that * denotes the discrete convolution in Eqn. 1.16.

An important issue arises due to the fact that non-Cartesian data can be acquired with a varying sampling density. For example, the data points in spiral sampling are acquired with a significantly higher density in the central parts of the k-space. If this is not accounted for, it leads to images with a noticeable overweighting of low k-space frequencies. So, each sample point has to be weighted with a density compensation function DCF (kj), which is a measure of the inverse of the k-space sampling density.

$$\boldsymbol{R_C(k) = \sum_j (DCF(kj).W(kj)) * C(k)} \qquad [\mathbf{1}.17]$$

In Eqn. 1.17, $R_C(k)$ denotes regridded Cartesian k-space data that was obtained from density compensated non-Cartesian data. A reconstructed 1D image signal S(x) from density compensated and regridded data can then be obtained by means of an inverse discrete Fourier transform ($\mathcal{F}^{-1}$).

$$\boldsymbol{S}(\boldsymbol{x}) = \boldsymbol{\mathcal{F}}^{-\mathbf{1}}\left\{\left(\boldsymbol{DCF}\left(\boldsymbol{K}_j\right).\boldsymbol{W}(\boldsymbol{kj})\right) * \boldsymbol{C}(\boldsymbol{k})\right\} \qquad [\mathbf{1}.18]$$

In general, numerical or analytical estimations are needed to evaluate the sampling density. The most widely used approach in MR image reconstruction is described in different lituratures [20, 18, 16].

1.4. Statement of the problem

The development and optimization of the MRF process are time-consuming, expensive which requisite repetitive experiment and often needs a synthetic phantom or human subject to test it on the real scanner and detect the results. Here we develop Simulation frameworks as an alternative to real-life experiments to study Multipart systems and physical phenomena of MRF under ideal/perfect and fully controlled conditions without the need for expensive materials using spiral undersampling.

1.5. Objectives of the Thesis

1.5.1. General Objective

The purpose of this thesis work was to provide a numerical simulation framework for magnetic resonance fingerprinting (MRF) using spiral undersampling.

1.5.2. Specific Objectives

- To build a dictionary of estimated signal evolutions for a given T1, T2, and Off-resonance values.
- Extend the existing simulation and image reconstruction approach for use in magnetic resonance fingerprinting.
- Simulate the signal acquisition for a given trajectory and validate the pulse sequence design and sampling scheme.
- Perform matching between the acquired signal and the dictionary to build quantitative maps.

- Evaluation of spiral under sampling effect on Inversion Recovery Balanced Steady-State Free Precision (IR_BSSFP) MRF parameter map.
- Compare existing simulations with the proposed simulation scheme by generating parameter maps.
- Evaluating the effect of additive noise on the MRF parameter map with different levels of noise.

1.6. Scope and Delimitation of the Thesis

The work is limited to a simulation framework only and no data has been acquired in the real environment using MRI scanners.

1.7. Organization of Thesis

The rest of the thesis has been organized into five chapters. Chapter 2 summarizes the basics of the T1 and T2 quantification. It starts with a comparison of quantitative versus qualitative imaging techniques. The rest of the chapter summarizes the conventional as well as current popular methods of measuring T1 and T2. Chapters 3 offers a detailed description of the MRF method focuses on introducing the basic MRF concept, including methods of developing each step of the MRF concept. Chapters 4 give a detailed explanation of the proposed simulation and comparison against existing simulations. Chapter 5 summarizes the results of the different experiments and some important discussions. Chapter 6 concludes the thesis by incorporating a discussion on future works.

Chapter 2 : **Parametric Imaging**

2.1. Conventional Quantitative Imaging

Conventional MR images (T1 and T2 weighted images) have worthy tissue contrast which is based on properties of human tissues including proton density, relaxation times, and susceptibility. Since the image intensity reflects the effect of factors being combined, the intensity itself is difficult to contain certain biophysical information of tissue alone. Therefore, diagnosis based on conventional MR images depends heavily on the contrast between different anatomies, and it is also dependent on the proficiency of the clinicians diagnosing the subject. In quantitative MRI, information related to the function and structure is often directly reflected within the image intensity. The disease-causing environmental changes of tissues cause changes in relaxation times of T1 and T2, which can be quantitatively measured and visualized as parameter maps. This quantified information enables longitudinal study and comparability between patients. The gold standard methods include the inversion recovery (IR) experiment for the measurement of T1, saturation recovery look-locker (SRLL), variable flip angle spoiled gradient recalled method (driven equilibrium single pulse observation of T1), and variable flip angle steady-state free precession method (driven equilibrium single pulse observation of T2). Because of the diagnostic potential of T1 and T2, many quantitative methods have been developed. The standard measurements of T1 and T2 are not clinically feasible because they suffer from long acquisition times.

2.1.1. Single Parametric Imaging

2.1.1.1. T1 Mapping Using Saturation Recovery Look-Locker Sequence

The sequence of SRLL as described in [21] uses three non-slice-selective 90° RF pulses applied at the start of the sequence to saturate longitudinal magnetization. Then N time points with constant interval τ along the recovery curve are sampled using fast low-angle shot (FLASH). For better exactness of curve fitting, a sample time range covering 85% recovery of longitudinal magnetization is recommended. A TR long enough for full T1 relaxation is required between two saturations, typically five times the longest T1.

The longitudinal magnetization before each excitation pulse in FLASH has the same form as IR, however, effective longitudinal relaxation time ${T_1}^*$ instead of $T1$, and effective equilibrium longitudinal magnetization M^* instead of $M(0)$ are used in this model. The signal evolution in Look-Locker acquisition has been derived in [22].

$$\boldsymbol{M(n) = M^* - \left(M^* - M(0)\right)e^{\left(-\frac{n\tau}{T_1{}^*}\right)}\ , n = 1, 2, \dots, N} \qquad [\mathbf{2.1}]$$

where M (0) is the initial longitudinal magnetization instantly after the saturation pulses and is nearly zero. M^* is the effective equilibrium longitudinal magnetization and is related to the equilibrium longitudinal magnetization M_0 by:

$$\boldsymbol{M^* = M_0 \frac{1 - e^{\left(\frac{-\tau}{T_1}\right)}}{1 - e^{\left(\frac{-\tau}{T_1{}^*}\right)}}} \qquad [\mathbf{2.2}]$$

Using the first-order Taylor expansion of $e^{\left(\frac{-\tau}{T_1}\right)}$ and $e^{\left(\frac{-\tau}{T_1{}^*}\right)}$

$$\boldsymbol{e^{\left(\frac{-\tau}{T_1{}^*}\right)} = 1 - \frac{\tau}{T_1{}^*} + \cdots} \qquad [\mathbf{2.3}]$$

$$\boldsymbol{e^{\left(\frac{-\tau}{T_1}\right)} = 1 - \frac{\tau}{T_1} + \cdots} \qquad [\mathbf{2.4}]$$

Using the above equation, the relationship between $M0$, M^* $T1$, $T_1{}^*$ can be expressed as:

$$\boldsymbol{T_1 = \frac{M_0}{M^*} T_1{}^*} \qquad [\mathbf{2.5}]$$

Mo can be derived with a single FLASH scan with TR longer than five times the longest T1. T1 mapping can be performed in the following procedure: use three-parameter curve fitting to estimate M^*, M^*- M (0), and $T_1{}^*$ in Eqn. (2.1), then $T1$ can be derived from its relationship with $M0$, M^*, $T_1{}^*$in Eqn. (2.5).

2.1.1.2. Variable Flip Angle Spoiled Gradient Recalled Method (DESPOT1)

There are different ways of quantifying T1 relaxation times by sampling the recovery of the longitudinal magnetization following an inversion or saturation preparation pulse. Here T1 relaxation time is quantified through the application of repeated RF pulses with constant inter-pulse delay, TR, and complete spoiling of the transverse magnetization which led the spin system to adynamic equilibrium that depends on T1 [23, 24]:

$$\boldsymbol{S_{SPGR} = PD \frac{1 - e^{-\frac{TR}{T1}}}{1 - e^{-\frac{TR}{T1}} cos\alpha} sin\alpha} \qquad [\mathbf{2.6}]$$

where S_{SPGR} is the spoiled gradient recalled (SPGR) signal intensity associated with flip angle, PD is a factor proportional to the equilibrium longitudinal magnetization:

$$\boldsymbol{\frac{S_{SPGR}}{sin\alpha} = \frac{S_{SPGR}}{tan\alpha} e^{-\frac{TR}{T1}} + PD\left(1 - e^{-\frac{TR}{T1}}\right) \qquad [2.7]}$$

Here T1 can be calculated directly from the slope of the $\frac{S_{SPGR}}{sin\alpha}$ versus $\frac{S_{SPGR}}{tan\alpha}$ line

$$\boldsymbol{T1 = -TR/\, ln(slope) \qquad [2.8]}$$

2.1.1.3. Variable Flip Angle Steady-state Free Precession Method (DESPOT2)

Unlike DESPOT1, variable flip angle steady-state free precession or DESPOT2 uses variable flip angle true fast imaging with steady-state (true FISP) or balanced steady-state free precession (BSSFP) [2] to determine T2 values. Unlike SPGR in which the transverse magnetization is completely spoiled before each RF pulse allowing only the longitudinal magnetization to reach equilibrium, in BSSFP the transverse magnetization is focused before each excitation, making all gradient balanced. This means the net gradient area and moment across each TR is zero and both the longitudinal and transversal magnetization are brought into dynamic equilibrium [23, 25, 24] which is a complex mixture of T1, T2, proton density, and off-resonance.

$$\boldsymbol{S_{ssfp} = PD\frac{\left(1 - e^{-\frac{TR}{T1}}\right) sin\alpha}{1 - e^{-\frac{TR}{T1}} e^{-\frac{TR}{T2}} - \left(e^{-\frac{TR}{T1}} - e^{-\frac{TR}{T2}}\right) cos\alpha} \qquad [2.9]}$$

$$\boldsymbol{\frac{S_{ssfp}}{sin\alpha} = \left(\frac{e^{-\frac{TR}{T1}} - e^{-\frac{TR}{T2}}}{1 - e^{-\frac{TR}{T1}} e^{-\frac{TR}{T2}}}\right)\frac{S_{ssfp}}{tan\alpha} + \frac{PD\left(1 - e^{-\frac{TR}{T1}}\right)}{1 - e^{-\frac{TR}{T1}} e^{-\frac{TR}{T2}}} \qquad [2.10]}$$

Outlining $\frac{S_{ssfp}}{sin\alpha}$ versus $\frac{S_{ssfp}}{tan\alpha}$ and making use of the $T1$ information obtained formerly with DESPOT1 allows the computation of T2 as:

$$\boldsymbol{T2 = \frac{-TR}{ln\left[\left(slope - e^{-\frac{TR}{T1}}\right)/\left(slope * e^{-\frac{TR}{T1}} - 1\right)\right]} \qquad [2.11]}$$

2.1.2. Multiple Parametric Imaging

The above method for the quantification of relaxation time used two separate experiments for each quantification of relaxation time. But multi-parametric methods quantify multiple parameters like T1, T2, and M0 in a single acquisition. Generation of proton density, T1, and T2 maps follow from IR True FISP data acquired along a golden angle radial trajectory [26] since it uses sequences from which the signal is a combined function of multiple parameters. The IR True FISP signal after nTR scan can be described by a three-parameter exponential, as described in [27]:

$$\boldsymbol{S(n.TR) = S_{stst} - (S_0 + S_{stst}).\, e^{\left(\frac{(-n.TR)}{T_1{}^{*}}\right)}} \qquad [\mathbf{2.12}]$$

where S_{stst} is the steady-state signal; S_0 is the transient state signal extrapolated to t = 0; and ${T_1}^{*}$ is the apparent relaxation time.

T1, T2, and M0 can then be obtained from the three fit parameters S_{stst}, S_0, and ${T_1}^{*}$, and the excitation flip angle α, with the assumption that TR is much less than T2, according to [28, 27]:

$$\boldsymbol{T_1 = \frac{{T_1}^{*}\,\frac{S_0}{S_{stst}}\,cos\alpha}{2}} \qquad [\mathbf{2.13}]$$

$$\boldsymbol{T_2 = {T_1}^{*}\, sin^2\, \alpha/2 \left(1 - \frac{S_{stst}}{S_0} cos\alpha/2\right)^{-1}} \qquad [\mathbf{2.14}]$$

$$\boldsymbol{M_0 = \frac{S_0}{sin\alpha/2}} \qquad [\mathbf{2.15}]$$

Chapter 3 : **Magnetic Resonance Fingerprinting**

Quantitative magnetic resonance imaging (QMRI) affords an effective tool for measuring several basic NMR properties of tissues such as the T1 and T2 relaxation times, field inhomogeneity, diffusion, perfusion, and magnetic transfer [3]. In spite of being the long-term goal of the MRI community, current quantitative approaches are enormously time inefficient and for this reason not clinically applicable. Standard QMRI approaches [21, 23, 24, 25, 26] acquire a large sequence of images at a different time and use a curve-fitting tool for parameter estimation for each image pixel. This procedure runs separately to estimate each parameter which makes it difficult for applicability in clinical settings.

Magnetic Resonance Fingerprinting (MRF) is a high-speed imaging technique for the quantification of multiple tissue properties such as proton density (PD), relaxation times, and field inhomogeneity [5]. Some of these parameters can be obtained simultaneously over a minute. Utilizing a variable series of flip angles (FAs) and repetition times (TRs) makes the signal in the transient state and a unique ‘fingerprint’ is generated corresponding to the parameters. Different kinds of pulse sequences can be used such as balanced steady-state free precession (bSSFP) [5], fast imaging with steady-state free precession (FISP) [29] , and quick echo splitting NMR technique (QUEST) [30] depending on the needs.

The developed fingerprints are then matched to a pre-generated dictionary, producing the best-fit combination of tissue properties. The highly under-sampled spiral trajectory is used as a sampling scheme to step up scan time. The spatially under-sampled artifacts manipulated to be incoherent over time are compensated by surplus temporal data during the matching process. This concept gives a high degree of freedom to the pulse sequence modification, signal generation, data acquisition, and post-processing.

Generally, three key principles are behind MRF (see also Fig. 2):

- Applying one excitation sequence that simultaneously encodes many quantitative parameters of interest.
- Using more complicated but shorter excitation patterns than those used in conventional Q-MRI schemes, and finally
- Considerable under-sampling of the k-space data at each temporal frame.

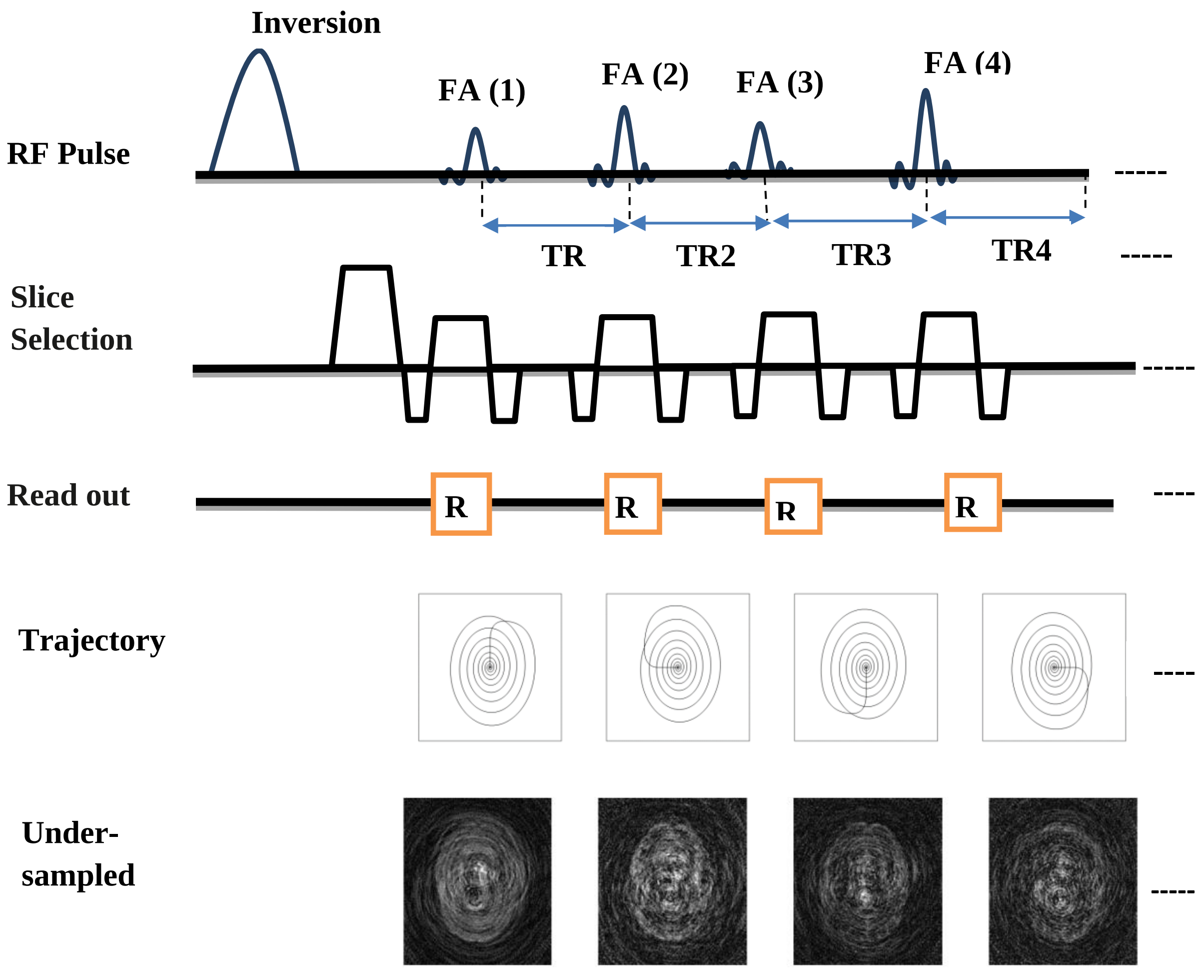

Figure 2: Sequence diagram showing the excitation pulses, slice selection gradients, readouts, the k-space trajectory for each TR, and the resulting under-sampled images.

3.1. Methodology

3.1.1. Pulse Sequence

One cause of the time-consuming MR scan is the long TR that waits for the full decay of the transverse magnetization and full recovery of the longitudinal magnetization, so at each image acquisition, the signal intensity starts at the same equilibrium. The steady-state free precession (SSFP) signal state happens by exposing a nuclear spin system to a series of short and equally spaced RF pulses [2]. When the spacing of the RF pulses or TR is much shorter than T2, a dynamic equilibrium state with high SNR could be established. For this reason, SSFP sequences have been used to drastically reduce the scan time. There are three main groups of the SSFP sequence [2].

- Uses both RF and gradient spoiling (spoiled gradient echo, also known as Fast Low Angle Shot MRI (FLASH));

- Applies gradient spoiling gradient with no RF spoiling (Fast Imaging with Steady Precession (FISP));
- Balanced SSPF (bSSFP) uses coherent RF phase and balanced gradients where the net effect of gradients in each encoding direction is zero.

MRF acquisition based on an IR-bSSFP sequence was employed (as in Fig. 2). This choice of the basic pulse sequence is based on its sensitivity to T1, T2, and off-resonance [5].

The flip angles (FAs) and the repetition times (TRs) are designed to generate different signal shapes for different tissue types to quantify the relaxation parameters and to have smoothly varied signals. The FA is designed as it is described in [5] which is smoothly changing FA with the added value of some random coefficient.

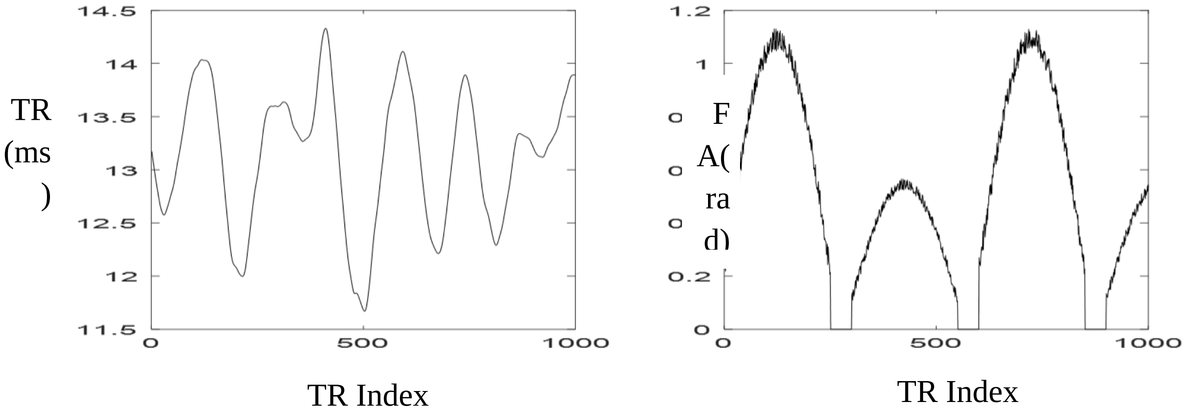

Figure 3 Examples of the first 1000 points of flip angle (FA) pattern (left) and repetition time (right).

$$\boldsymbol{FA_j(n)} = \begin{cases} \boldsymbol{50\,sin\left(2\pi\, {}^{n}\!/_{500}\right) + random(5)} & \boldsymbol{,j\ odd} \\ \boldsymbol{25\,sin\left(2\pi\, {}^{n}\!/_{500}\right) + random(5)} & \boldsymbol{,j\ even} \end{cases} \qquad [3.1]$$

where j = 1,2,3,4, and n = 1,2,3, … ,250.

As Fig. 3 shows FA pattern consists of half-sinusoidal curves with a period of 250 repetition times followed by no excitations (delay time) for 50 repetition times between the cycles to allow uninterrupted relaxation. The maximum flip angles alter between 70◦ and 30◦ in odd and even periods. Noise with zero mean which is uniformly distributed with a standard deviation of 5 was added. An inversion pulse was applied at the beginning of the sequence to enhance T1 sensitivity. The inversion pulse was followed by fingerprint simulation consisted of four parts with varied FA and TR (Fig. 3). In each of the first three parts, a total of 250 frames were acquired with the FA sinusoidally ramped up and then ramped down. In the last part, only 100 frames were acquired with the FA sinusoidally ramped up.

3.1.2. Spiral Trajectory Design

To make MRF acquisition faster, we use the acceleration factor by using the under-sampling capability of MRF sequences with variable density spiral trajectories. Although there are many ways of generating spiral trajectories [13, 16, 15], the trajectory was based on the method proposed by Kim et al. [12]. The spiral trajectories used were designed to have zeroth moment compensation so that $Mo = \int_0^T G(t)dt = 0$ based on Krishna. S et al. [31]. The spiral trajectory is designed for a specific field of view, image size, and restricted by maximum gradient amplitude and maximum slew rate. The spiral trajectory is expressed as:

$$\boldsymbol{K(\tau) = K_{max}\,\tau^{\alpha} e^{j\omega\tau}} \qquad [\mathbf{3.2}]$$

where $\tau \in [0, 1]$ is a function of time, $\omega = 2\pi n$ and n is the number of turns. When $\alpha > 1$, the trajectory will oversample inner k-space and under-sample outer kspace. α can be chosen depending on the amount of oversampling needed in the center. Constant density spirals are achieved when $\alpha = 1$, while a trajectory with oversampling in high k-space values can be achieved with $\alpha < 1$. The amplitude and slew rate of the gradient at different times are dependent on τ and follow the method described by Hardy *et* al. [32].

$$\boldsymbol{g(t) = \frac{1}{\gamma}\frac{dk}{d\tau}\frac{d\tau}{dt}} \qquad [\mathbf{3.3}]$$

$$\boldsymbol{SR(t) = g(t)' = \frac{1}{\gamma}\left[\left(\frac{d\tau}{dt}\right)^2 \frac{d^2\tau}{d\tau^2} + \frac{dk}{d\tau}\,\frac{d^2\tau}{d\tau^2}\right]} \qquad \mathbf{[3.4]}$$

where γ is the gyromagnetic ratio. In the amplitude-limited case, by using maximal gradient g_m,

$$\boldsymbol{\tau(t) = \left[\frac{\gamma g_m}{k_{max}\omega}(\alpha + 1)t\right]^{1/(\alpha+1)}} \qquad \mathbf{[3.5]}$$

τ will increase to 1 at ending time Tea calculated as follows:

$$\boldsymbol{T_{ea} = \left[\frac{\gamma g_m}{k_{max}\omega}(\alpha + 1)t\right]^{-1}} \qquad [\mathbf{3.6}]$$

In the slew-rate-limited case, by using maximal slew rate $SR_m = \frac{dg}{dt}$

$$\boldsymbol{\tau(t)} = \left[\sqrt{\frac{\gamma SR_m}{k_{max}\omega^2}}\left({}^{\alpha}\!/_{2} + 1\right)\right]^{1/\left({}^{\alpha}\!/_{2}+1\right)} \qquad \textbf{[3.7]}$$

τ will increase to 1 at ending time Tes calculated as below

$$T_{es} = \left[\sqrt{\frac{\gamma SR_m}{k_{max}\omega^2}}\left({}^{\alpha}\!/_{2} + 1\right)\right]^{-1} \qquad \textbf{[3.8]}$$

The above two cases can be combined to satisfy both the slew-rate and amplitude constraints. A typical trajectory will start in the slew-rate limited and it will switch to the amplitude limited regions. The transition time ($t = T_{s2a}$) can be found by setting $g(t) = g_m$ in the slew-rate limited region.

$$T_{s2a} = \left[\frac{g_m\gamma}{k_{max}\frac{1}{{}^{\alpha}\!/_{2}+1}\left(\left({}^{\alpha}\!/_{2} + 1\right)\sqrt{\frac{\gamma SR_m}{k_{max}\omega^2}}\right)^{\left[{}^{(\alpha+1)}\!/_{{}^{\alpha}\!/_{2}+1}\right]}}\right]^{(\alpha+2)/\alpha} \qquad [\mathbf{3.9}]$$

Finally, the analytic variable density spiral can be organized like:

$$\boldsymbol{\tau(t)} = \begin{cases} \left[\sqrt{\frac{S_m\gamma}{K_{max}\omega^2}}\left(\frac{\alpha}{2}+1\right)t\right]^{\left[1/\frac{\alpha}{2}+1\right]} & (0 \le\ t \le min(T_{s2a},\ T_{es}\ )) \\ \left[\frac{\gamma g_m}{K_{max}\omega}(\alpha+1)t\right]^{1/(\alpha+1)} & (T_{s2a} \le t \le\ \ T_{es}\ ) \end{cases} \qquad \textbf{[3.10]}$$

The value of ***n*** can also be found by Nyquist sampling distance between adjacent trajectory turns. Therefore, the field of view constraint has to satisfy $\mathbf{k(1) - k\left(\frac{n-1}{n}\right) \le\ 1/FOV}$, hence the solution for ***n*** becomes:

$$\boldsymbol{n} = \left[1 - (1 - 2/N)^{\frac{1}{\alpha}}\right]^{-1} \qquad \textbf{[3.11]}$$

The designed spiral trajectory has FOV of 30 cm, a matrix size of 256×256, and 5 microsecond sampling period with 1104 points per each single interleave without including the rewinder. During the simulation, the spiral trajectory was rotated 15° from one to the next. The simulation was repeated 24 times, with 24 evenly distributed spiral interleaves to fully cover the k-space. As the designed trajectory fully sample the entire k-space with 24 interleaves, corresponding to 15° rotation between each interleave. For the spiral design the gradient characteristics of amplitude 4 G/cm, slew rate: 17 G/cm/ms was used. Figure 4 depicts the k-space trajectory as well as the variation of the k-space, gradient, and slew rates with respect to time.

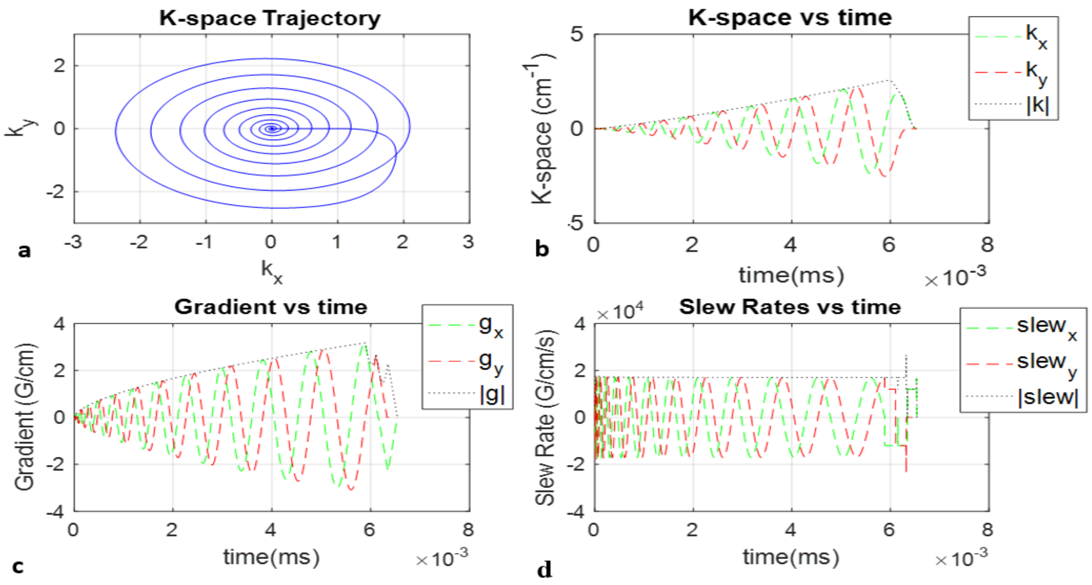

Figure 4: Design a spiral trajectory as (a), k-space (b), gradient (c), and slew rate (d).

3.1.3. Dictionary Simulation

The Bloch equations used for MRI simulations give the time evolution of a spin magnetization vector M = (Mx, My, Mz) at a given position (x, y, z) by:

$$\boldsymbol{\frac{dM}{dt} = \gamma.(M \times B) - \left\{\begin{matrix} \frac{Mx}{T2} \\ \frac{My}{T2} \\ \frac{Mz - Mo}{T1} \end{matrix}\right\}} \qquad [\mathbf{3.12}]$$

Solving the above equation

$$\frac{d}{dt}\begin{bmatrix} \mathrm{Mx} \\ \mathrm{My} \\ \mathrm{Mz} \end{bmatrix} = \gamma \begin{bmatrix} \mathrm{MyB_0 - Mz} \\ \mathrm{-MxB_0 + MzB_x} \\ \mathrm{MxB_y(t) - MyB_x} \end{bmatrix} - \begin{bmatrix} \frac{1}{\mathrm{T_2}}\mathrm{Mx} \\ \frac{1}{\mathrm{T_2}}\mathrm{My} \\ \frac{1}{\mathrm{T_1}}(\mathrm{Mz - M_0}) \end{bmatrix} \qquad [\mathbf{3.13}]$$

$$\boldsymbol{M_X(t) = e^{-t/T_2}\left[M_X(0)\cos(\Delta\omega t) + M_y(0)\sin(\Delta\omega t)\right]} \qquad [\mathbf{3.14}]$$

$$\boldsymbol{M_y(t) = e^{-t/T_2}\left[-M_X(0)\,sin(\Delta\omega t) + M_y(0)\,cos(\Delta\omega t)\right]} \qquad [195]$$

$$\boldsymbol{M_z(t) = M_z(0)e^{-t/T_1} + M_z^0\left(1 - e^{-t/T_1}\right)} \qquad [\mathbf{3.16}]$$

The magnetization vector can be computed as:

$$\boldsymbol{M(r,t) = Rot(\theta_\beta)R_{relx}\,R_{rf}\,M(0)} \qquad [\mathbf{3.17}]$$

where **Rot ($\boldsymbol{\theta}$)** is a rotation matrix defined by: $\begin{bmatrix} \boldsymbol{cos\theta} & \boldsymbol{sin\theta} & \mathbf{0} \\ \boldsymbol{-sin\theta} & \boldsymbol{cos\theta} & \mathbf{0} \\ \mathbf{0} & \mathbf{0} & \mathbf{1} \end{bmatrix}$

$\boldsymbol{\theta_\beta}$ is related to off-resonance **($\boldsymbol{\Delta\omega}$)** as**:** $\boldsymbol{\theta_\beta = \gamma\Delta\omega TR}$

$\boldsymbol{R}_{\mathbf{relx}}$ describes the relaxation effect and is given by.

$$\boldsymbol{R}_{\mathbf{relx}} = \begin{bmatrix} \boldsymbol{e^{\frac{TR}{T2}}} & \mathbf{0} & \mathbf{0} \\ \mathbf{0} & \boldsymbol{e^{\frac{TR}{T2}}} & \mathbf{0} \\ \mathbf{0} & \mathbf{0} & \boldsymbol{e^{\frac{TR}{T1}}} \end{bmatrix} + \begin{bmatrix} \mathbf{0} \\ \mathbf{0} \\ \mathbf{1} - \boldsymbol{e^{\frac{TR}{T1}}} \end{bmatrix}$$

$\boldsymbol{R}_{\mathbf{rf}}$ represents the rotating effect of an RF pulse with phase angle φ and flip angle α by:

$$\boldsymbol{R}_{\mathbf{rf}} = \mathbf{Rot}_{\boldsymbol{z}}(\boldsymbol{\varphi})\mathbf{Rot}_{\boldsymbol{x}}(\boldsymbol{\alpha})\mathbf{Rot}_{\boldsymbol{z}}(-\boldsymbol{\varphi})$$

$$\boldsymbol{R}_{\mathbf{rf}} = \begin{bmatrix} \cos\boldsymbol{\varphi} & \sin\boldsymbol{\varphi} & 0 \\ -\sin\boldsymbol{\varphi} & \cos\boldsymbol{\varphi} & 0 \\ 0 & 0 & 1 \end{bmatrix} \begin{bmatrix} 1 & 0 & 0 \\ 0 & \cos\alpha & -\sin\alpha \\ 0 & \sin\alpha & \cos\alpha \end{bmatrix} \begin{bmatrix} \cos\boldsymbol{\varphi} & -\sin\boldsymbol{\varphi} & 0 \\ \sin\boldsymbol{\varphi} & \cos\boldsymbol{\varphi} & 0 \\ 0 & 0 & 1 \end{bmatrix}$$

The inversion recovery balanced steady-state free precession (IR-BSSFP) dictionary used in the matching algorithm was simulated using Bloch simulation as described above with the flip angle and TR patterns in Fig. 3**.** Signal time courses with different sets of characteristic parameters (*T1, T2,* and off-resonance) were simulated as in the original MRF work [5] (see also Fig. 5).

Every dictionary fingerprint has its own unique T1, T2, and off-resonance (**B0**) values stored in a lookup table (LUT), represented as the matrix **LUT.**

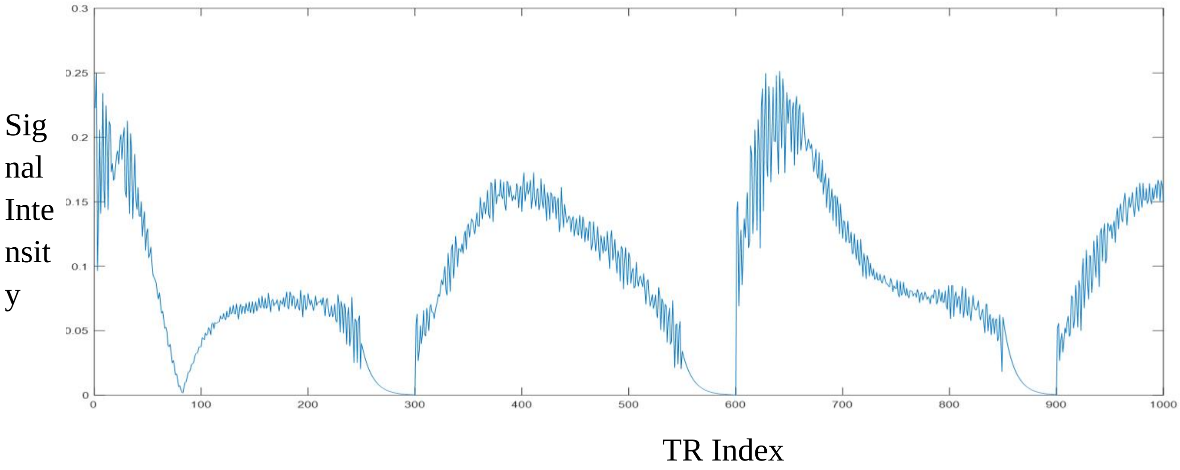

Figure 5: The IR-BSSFP dictionary generated from a set of pseudo-random FAs shown in Figure (3). This dictionary encodes T1 and T2 relaxation times and off-resonance frequency B0 (signal vs number of TRs).

3.1.4. Pattern Matching

In pattern matching one simulated tissue property is selected from dictionary entry for each measured pixel. Here dictionary and simulated image matching are done by calculating vector dot-product. The dictionary entry with the peak dot product value is nominated to represent the signal evolution. Once the vector dot-product is calculated the tissue properties like T_1 relaxation, T_2 relaxation, and off-resonance will be generated by mapping the matched value with the predefined lookup table.

$$\boldsymbol{Ki = argmax\frac{|\langle Dk, Xi, :\rangle|}{\|Dk\|_2}} \qquad [\mathbf{3.18}]$$

$$\boldsymbol{PD = argmax\frac{\langle Dki, Xi, :\rangle}{\|Dki\|_2^2}} \qquad [\mathbf{3.19}]$$

$$\boldsymbol{T1, T2, B0 \ = \ LUT(Ki)} \qquad [\mathbf{3.20}]$$

The parameters Ki are the matching dictionary indices. PD is the proton density and B0 is the off-resonance map. The parameter maps are extracted from LUT, which holds the values of T1, T2, and B0 for each Ki.

Chapter 4 : **Simulation Framework**

4.1. Simulation of Nuclear Magnetic Resonance Imaging

Numerical simulation of MRI experiments is a valuable tool for predicting outcomes of a proposed method before in vivo investigation. Simulation frameworks as an alternative to real-life experiments have several benefits and have been used since the invention of MRI. Multipart systems and physical phenomena can be studied under ideal/perfect and fully controlled conditions without the need for expensive materials. It can also be used as a tool to give students better awareness of a specific system and how different setups affect that system [7, 6]. MRF, being a favorable field of research in quantitative MRI, can aid from such simulation tools. Here we simulate serious of images which have a different fingerprint of specific tissues for the implementation of MRF with different pulse sequence, relaxation, spin density, and off-resonance values.

The simulation has different parts which consists of several sections. A pulse sequence part which allows the user to program a series of reputation time (TR) and RFpulses. The object offers options for choosing the type, size, and NMR characteristics of the object including T1, T2, spin density, and off-resonance. The image reconstruction section performs a non-uniform Fast Fourier Transform (NUFFT) operation on the data [17]. The block diagram in Fig. 6 illustrates the operations required to produce an MRF parameter map.

Signal values (both real and imaginary) are simulated at the read-out point and after some random noise is added to them passed into the image reconstruction algorithm. The main goal of the MRF simulator is to make the simulation as realistic as possible. So, it is important to provide as many different object and scanner related properties.

The simulation was done in MATLAB 2016b platform (MathWorks, Inc, Natick, MA), with a 2-GHz processor and 16 GB of memory, windows 10 operating system.

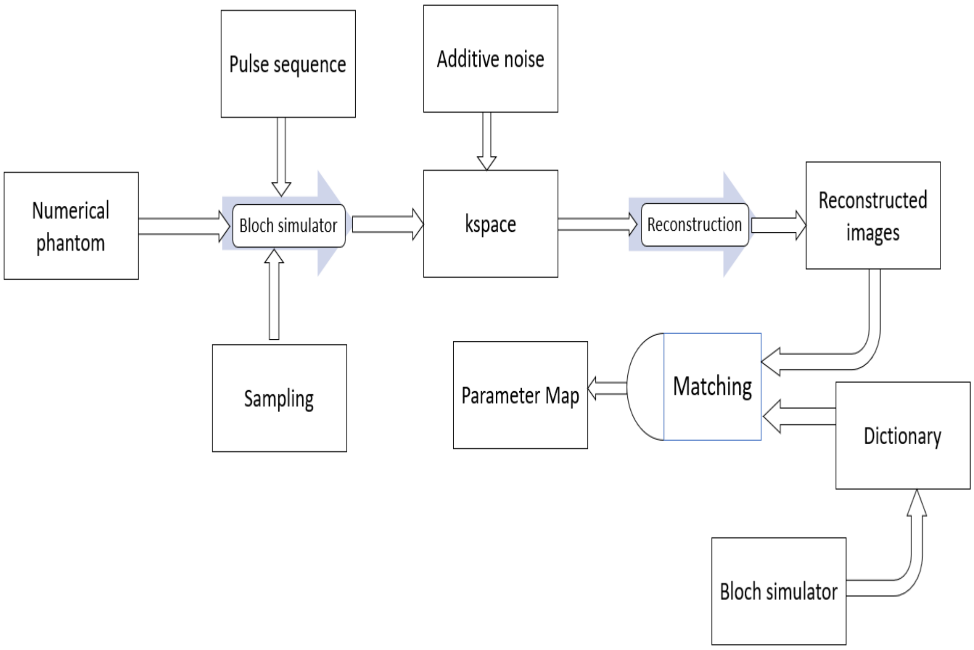

Figure 6: Block diagram of MRF simulator overview.

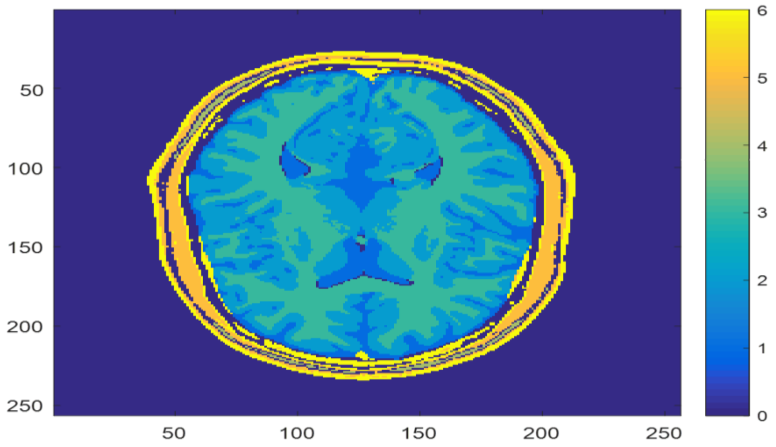

Figure 7: Segmented anatomical brain phantom stained by index:0=Background,1 =CSF, 2 =Grey Matter, 3 =White Matter, 4 =Fat, 5 =Muscle/Skin, 6 =Skin.

4.1.1. Object

There are two kinds of objects (numerical phantom) used in the simulation. The first object is generated using the digital brain phantom introduced by the McConnell Brain Imaging Centre, Montreal Neurological Institute (MNI), McGill University [33]. The digital brain phantom consists of a set of three-dimensional tissue, with nine tissue classes (white matter, gray matter, cerebrospinal fluid (CSF), fat, muscle, glial tissue, bone, skin, and connective tissue) [34] which is shown in Fig. 7. As used in [35, 36], six segments are used for the generation of ground truth object with slice number 80 which is depicted in Fig. 9. The pixels in the object contains a set of values necessary for the computation with the Bloch equations. These values are the proton density, off-resonance, and the two relaxation constants T1 and T2 as listed in Table 1. The second object or numerical phantom was generated using the custom phantom simulations shown in Fig. 8 with 6 circles for simulation using the values listed in Table 1 used for the verification of the simulation framework.

Tissue	Index	Proton density	T1(ms)	T2(ms)	Df (HZ)
Background	0	0	0	0	0
CSF	1	100	5012	512	50
Grey matter	2	100	1545	83	-30
White matter	3	80	811	77	20
Adipose	4	80	530	77	250
Skin/muscle	5/6	80	1425	41	250

Table 1: Tissue properties for MNI segmented brain phantom **[35]**.

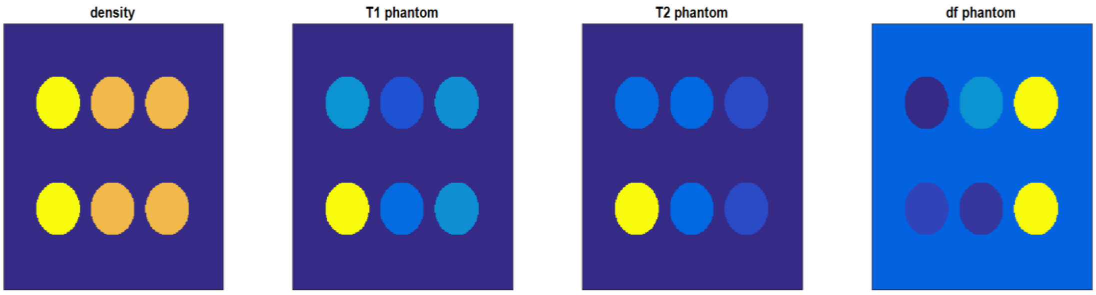

Figure 8: Ground truth images of custom phantom density, T1, T2, and off-resonance respectively which are used as input objects in matrix form for simulation of MRF image.

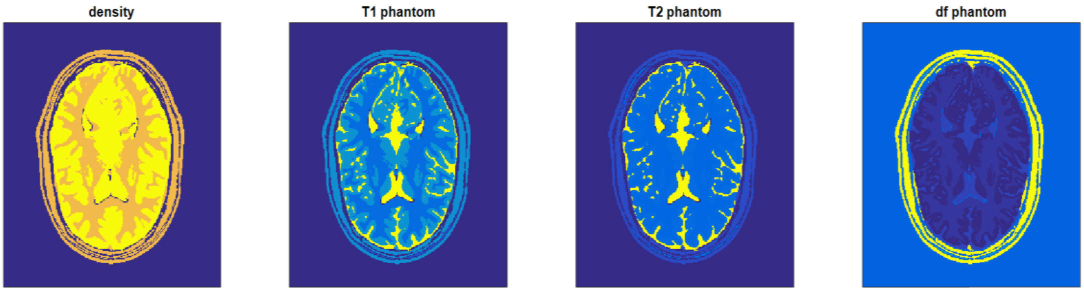

Figure 9: Ground truth images of MNI segmented brain phantom density, T1, T2, and off-resonance respectively which are used as input objects in matrix form for simulation of MRF image.

4.1.2. Bloch Simulator

The simulation of an MRI sequence is based on solving the 3D Bloch equation [8]. The Bloch equation used for MRI simulations is a linear differential equation that gives the time evolution of a spin magnetization vector M = (Mx, My, Mz) at a given position (x, y, z) by:

$$\frac{dM}{dt} = \gamma.(M \times B) - \left\{ \begin{matrix} \frac{Mx}{T2} \\ \frac{My}{T2} \\ \frac{Mz - M0}{T1} \end{matrix} \right\} \qquad [4.1]$$

where $M = (Mx, My, Mz)^T$ is the spin magnetization vector, $M0$ is the spin magnetization equilibrium value which depends on the proton density, (T1, T2) are the relaxation constants and γ is the gyromagnetic constant (42.58 MHz/T for Hydrogen proton).

The simulation implements a discrete-time solution of the Bloch equation [8] with the means of using rotation matrices and exponential scaling that depend on the sequence. The magnetization vector can be computed as:

$$\boldsymbol{M(r, t + \Delta t) = Rot(\theta_g) Rot(\theta_\beta) R_{relx}\, R_{rf}\, M(r, t)} \qquad [\mathbf{4.2}]$$

where Rot $\boldsymbol{(\theta)}$ is a rotation matrix defined by: $\begin{bmatrix} \boldsymbol{cos\theta} & \boldsymbol{sin\theta} & \mathbf{0} \\ \boldsymbol{-sin\theta} & \boldsymbol{cos\theta} & \mathbf{0} \\ \mathbf{0} & \mathbf{0} & \mathbf{1} \end{bmatrix}$

where $\boldsymbol{\theta_g}$ is linked to the applied gradient *G*(*t*) and $\boldsymbol{\theta_\beta}$ is related to off-resonance $\boldsymbol{(\Delta\omega)}$

$$\boldsymbol{\theta_g = \gamma r \int_0^t g(\tau)\, d\tau\,,\;\; \theta_\beta = \gamma \Delta\omega \Delta t} \;\;,$$

$\boldsymbol{R}_{\mathbf{relx}}$ describes the relaxation effect:

$$\boldsymbol{R}_{\mathbf{relx}} = \begin{bmatrix} \boldsymbol{e^{\frac{\Delta t}{T2}}} & \mathbf{0} & \mathbf{0} \\ \mathbf{0} & \boldsymbol{e^{\frac{\Delta t}{T2}}} & \mathbf{0} \\ \mathbf{0} & \mathbf{0} & \boldsymbol{e^{\frac{\Delta t}{T1}}} \end{bmatrix} + \begin{bmatrix} \mathbf{0} \\ \mathbf{0} \\ \mathbf{1} - \boldsymbol{e^{\frac{\Delta t}{T1}}} \end{bmatrix}$$

$\boldsymbol{R}_{\mathbf{rf}}$ represents the rotating effect of an RF pulse with phase angle φ and flip angle α by:

$$\boldsymbol{R}_{\mathbf{rf}} = \mathbf{Rot}_z(\boldsymbol{\varphi})\mathbf{Rot}_x(\boldsymbol{\alpha})\mathbf{Rot}_z(-\boldsymbol{\varphi})$$

$$\boldsymbol{R}_{\mathbf{rf}} = \begin{bmatrix} \cos\boldsymbol{\varphi} & \sin\boldsymbol{\varphi} & 0 \\ -\sin\boldsymbol{\varphi} & \cos\boldsymbol{\varphi} & 0 \\ 0 & 0 & 1 \end{bmatrix} \begin{bmatrix} 1 & 0 & 0 \\ 0 & \cos\alpha & -\sin\alpha \\ 0 & \sin\alpha & \cos\alpha \end{bmatrix} \begin{bmatrix} \cos\boldsymbol{\varphi} & -\sin\boldsymbol{\varphi} & 0 \\ \sin\boldsymbol{\varphi} & \cos\boldsymbol{\varphi} & 0 \\ 0 & 0 & 1 \end{bmatrix}$$

$$\boldsymbol{R}_{\mathbf{rf}} = \begin{Bmatrix} cos^2\boldsymbol{\varphi} + sin^2\boldsymbol{\varphi}\cos\alpha & sin\boldsymbol{\varphi}\mathbf{cos}\boldsymbol{\varphi}(\mathbf{1} - \mathbf{cos}\boldsymbol{\alpha}) & -sin\boldsymbol{\varphi}\mathbf{sin}\boldsymbol{\alpha} \\ sin\boldsymbol{\varphi}\mathbf{cos}\boldsymbol{\varphi}(\mathbf{1} - \mathbf{cos}\boldsymbol{\alpha}) & sin^2\boldsymbol{\varphi} + cos^2\boldsymbol{\varphi}\cos\alpha & cos\boldsymbol{\varphi}\mathbf{sin}\boldsymbol{\alpha} \\ sin\boldsymbol{\varphi}\mathbf{cos}\boldsymbol{\alpha} & -cos\boldsymbol{\varphi}\mathbf{sin}\boldsymbol{\alpha} & cos\alpha \end{Bmatrix}$$

The sampled points can be obtained by summation of the magnetizations along the XY plane

$$\boldsymbol{S}(\boldsymbol{t}) = \sum \boldsymbol{M}(\boldsymbol{t})\boldsymbol{x} + \boldsymbol{j}\sum \boldsymbol{M}(\boldsymbol{t})\boldsymbol{y} \qquad [\mathbf{4.3}]$$

4.1.3. Pulse Sequence

The flip angles (FAs) and the repetition times (TRs) are designed as it is introduced in section 2.2.1 to generate different signal shapes for different tissue types to quantify the relaxation parameters and to have smoothly varied signals. The FAs and TRs are designed as it is described in [5]; smoothly changing FA as shown in Fig. 3 with the added value of some random coefficients and variable TRs varying from 12 to 14 ms.

4.1.4. Sampling Scheme

As it is introduced in section 1.3, sampling can be designed based on the need for the specific MRI measurement depending on the pulse sequence used. There are different kinds of sampling techniques that can be used like Cartesian (linear sampling), Echo planner imaging (EPI), radial and spiral sampling. To make MRF acquisition faster, we use the acceleration factor by using the under-sampling capability of MRF sequences with variable density spiral trajectories. There are many ways of generating a spiral trajectory [13, 15, 16]. The trajectory used in this thesis was based on the method proposed by Kim et al. [12]. The spiral trajectories used were designed to have zeroth moment compensation so that $Mo = \int_0^T G(t)dt = 0$ based on Krishna. S et al. [31]. The designed trajectory has field of view (FOV) 30 cm, matrix size 256×256, and 5 microsecond sampling periods with 1104 sampling points per each single interleaves and a duration of 6 milliseconds. During the simulation, the spiral trajectory was rotated 15° from one to the next. The simulation was repeated 24 times, with 24 evenly distributed spiral interleaves to fully cover the k-space.

4.1.5. Image Reconstruction

Fast Fourier transform (FFT) is an exact fast algorithm to compute the discrete Fourier transform when data is acquired on an equally spaced grid-like Cartesian. But the sampling trajectory with a spiral that is irregularly distributed hinders the use of FFT. Reconstruction of data sampled with non-Cartesian trajectories involves additional postprocessing such as gridding because non-Cartesian trajectory data is not directly mapped to the grid of Cartesian k-space. The non-uniform fast Fourier transform (NUFFT) algorithm offers fast mapping for computing non-equally spaced sampling. Images from each simulation block were reconstructed separately using the NUFFT toolbox [17, 37]. Sampled data on all interleaves used in a one-time frame and corresponding sampling trajectory were the input to the toolbox. Before re-gridding, a density compensation function (dcf) is applied to non-Cartesian k-space data to gain even weighting across k-space and minimize reconstruction error [18]. The density compensation vector approach by Craig Meyer et al. [16] was used.

Let Y be the sampled data that is the out pout of the simulator, A^j the adjoint operator of NUFFT, and W_i the density compensation function. Then the reconstructed image X will be:

$$X = A^j(Y * W_i)$$

Here, the element-wise multiplication operator multiplies the data (Y) by the sampling density compensation function (W_i). In the first step, the non-uniform samples *Y* are convolved with an interpolation kernel *H* and resampled onto a Cartesian grid. The inverse FFT is then applied to the resampled data. A large interpolator size can achieve great accuracy for different kernels, at the cost of high memory usage and lower execution speed. To improve performance, a smaller kernel is preferred. Accurate results can be achieved using a kernel size of 6–7 using a min-max interpolator.

As it is shown in Fig. 10 and Fig. 11, the undersampled image with 6 interleaves and single-shot respectively show variable artifact effects and it can be shown more on the signal evolution of the time-series images.

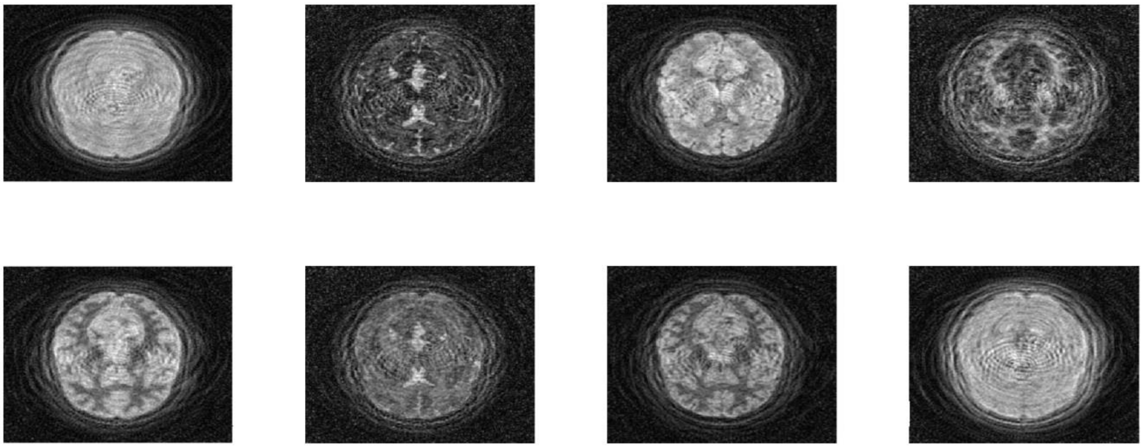

Figure 10: The first eight simulated images using the MRF simulator of unity resolution factor with 6 interleave.

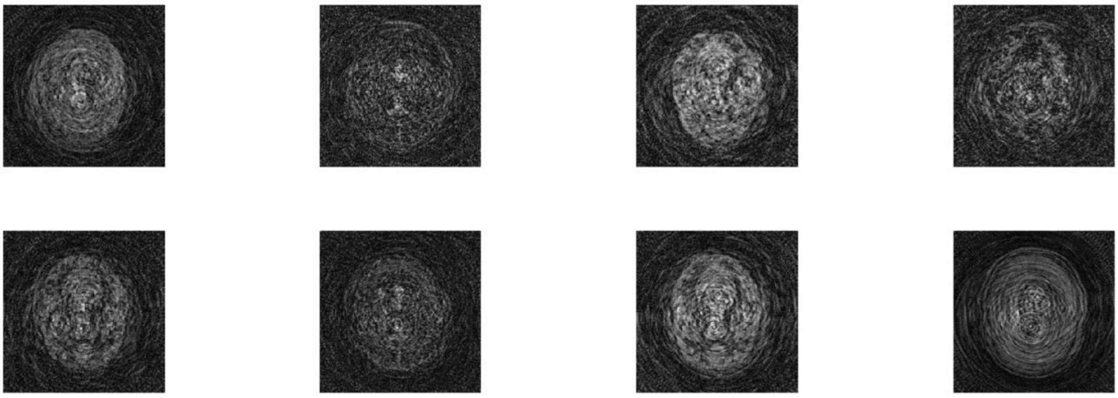

Figure 11 The first eight simulated images using the MRF simulator of unity resolution factor with single-shot.

4.2. Experimental Methodology

All experiments were done using two kinds of phantoms with spiral trajectories as a sampling technique since it is useful for the undersampling strategy to accelerate the MRF parameter quantification process. Imaging parameters for both phantom types were: FOV: 30×30 cm^2 and matrix size: 256×256. The designed spiral trajectory has FOV of 30 cm, a matrix size of 256×256, and 5 microsecond sampling period with 1104 points per each single interleave without including the rewinder. During the simulation, the spiral trajectory was rotated 15˚ from one to the next. The simulation was repeated 24 times, with 24 evenly distributed spiral interleaves to fully cover the k-space. The designed trajectory fully samples the entire k-space with 24 interleaves, corresponding to 15˚ rotation between each interleave. For the spiral design, the gradient characteristics were amplitude 4 G/cm and slew rate 17 G/cm/ms.

4.2.1. Evaluation of Undersampling Capability of MRF

The simulation was done using a full sample with 24 interleaves of variable density spiral on the two types of phantoms and the dictionary was simulated using similar sequences used in the simulation of images with T1, T2, DF values of the brain. To investigate the undersampling capability of each MRF sequence, the fully sampled data were retrospectively undersampled with the under-sample factor of 1, 4, 6, 8, 12, and 24.

4.2.2. Evaluating the Effects of Noise on the Parameter Map

Noise effect is unescapable in MRI due to different sources of noise. In MRI signals are mainly corrupted by thermal noise [38]. As used in different papers [39, 40, 41], the effects of noise on the parameter maps of MRF are evaluated by adding different levels of Gaussian noise to the real and imaginary parts of the simulated fingerprints distinctly and quantification errors are compared to the gold standard to evaluate which parameter map is affected more and which is less affected by the added noise. Here the effect of noise on the quantification of the parameter map is evaluated using three noise levels with SNR of 20.67, 14.65, and 10.2 dB using the brain phantoms.

4.2.3. Simulation Comparison

Different MRF papers [42, 35, 43, 36] were used to simulate MRF full sample image using Bloch simulation as described in section 3 without considering the effect of sampling gradient. That means the effect of sampling gradient is assumed negligible with a 256 × 256 slice from the segmented Brain web phantom [33] with segments corresponding to the background and six different tissues each with a set of T1, T2, B0, and PD values as it is listed in Table 1. To generate the ground truth and full sample MRF image, first 180-degree inversion pulse is applied, and a smoothly varying FA with varying TR [5] as in Figure 3 and echo time (TE) = TR/2 was used. The output of the Bloch response of the phantom segments is scaled by a proton density (PD) and generates the whole ground truth MRF image of size (Nx=256, Ny=256, L=1000) as seen in the first eight image in Figure 12 from the thousands. A similar sequence is used to generate a dictionary with specific combinations of parameters T1, T2, and B0 where T1 is greater than T2 around the value of the brain. Block diagram of the existing MRF simulator is shown in Fig. 13.

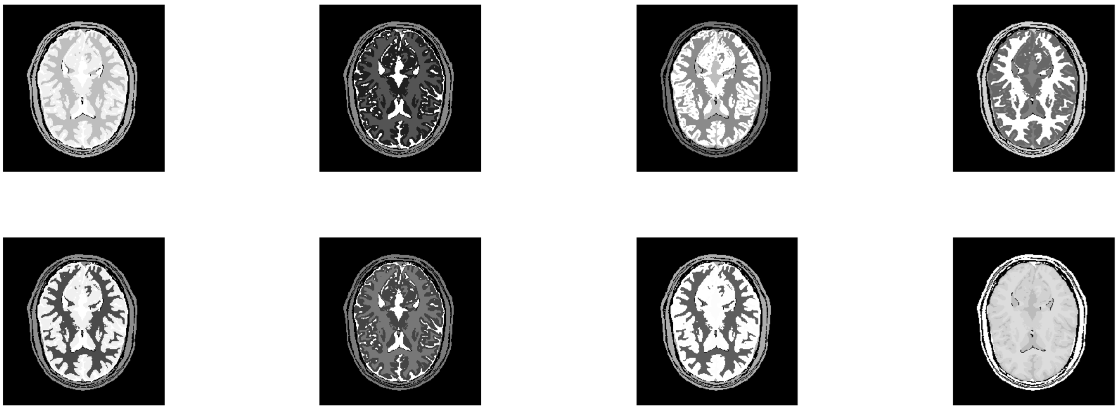

Figure 12: The first eight full sampled images using Bloch simulations without using sampling gradient assuming perfect sampling pattern.

After generating the fully sample MRF image shown in Fig. 12, the undersampled image is reconstructed using variable-density spiral (VDS) sampling [12] as shown in Fig. 14 and Fig. 15 using the NUFFT toolbox [17]. The reconstruction, as explained in section 1.33, has two steps. First, using the forward operator, the sampled points are calculated with the variable density spiral. Then, using the adjoint operator and the density compensation function, the undersampled image is reconstructed.

Let Ah be the forward operator and Aj the adjoint operator with density compensation [32] of W. Then:

$$X = Aj(diag(W)Ah)$$

where X is the reconstructed undersampled image.

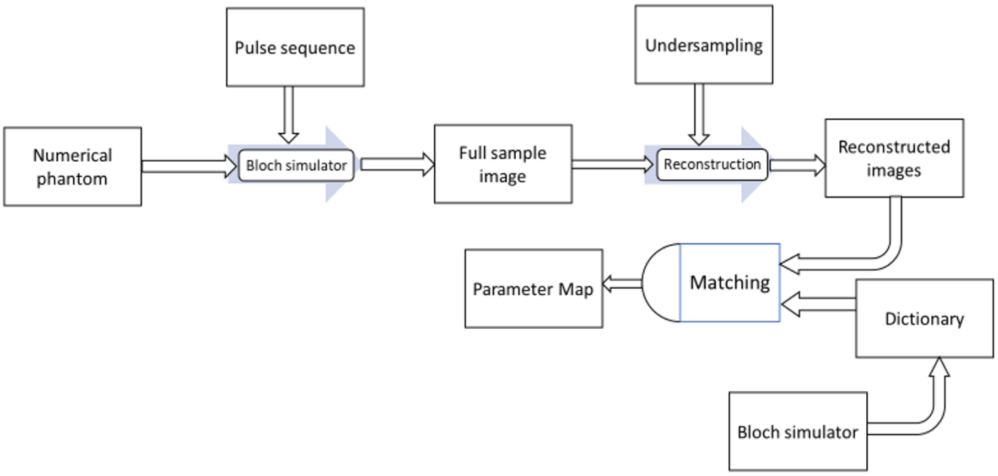

Figure 13: Block diagram of existing MRF simulator overview.

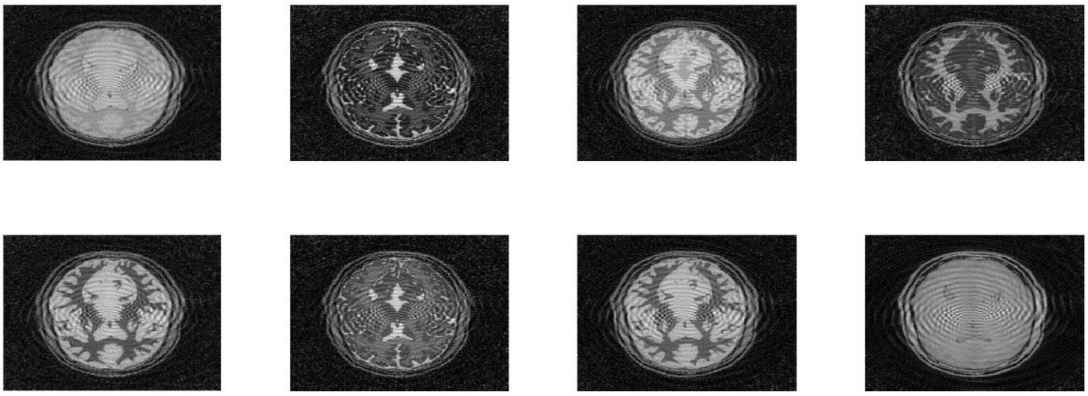

Figure 14: The first eight under-sampled images using 6 interleave variable density spiral sampling with the existing simulator.

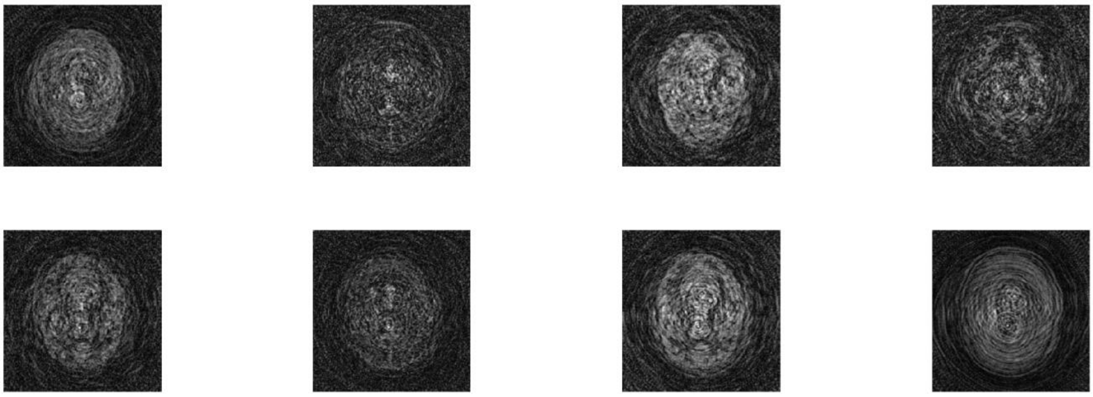

Figure 15: The first eight under-sampled images using a single interleave variable density spiral sampling with the existing simulator.

Chapter 5 : **Results and Discussion**

5.1. Results

In this thesis, two different objects were used for the simulation framework: simulated brain phantom object and custom generated phantom object. The use of these objects is to validate the simulation for the MRF Parameter mapping process. The dictionary was computed in approximately less than 5 minutes using a standard computer (see Fig.16).

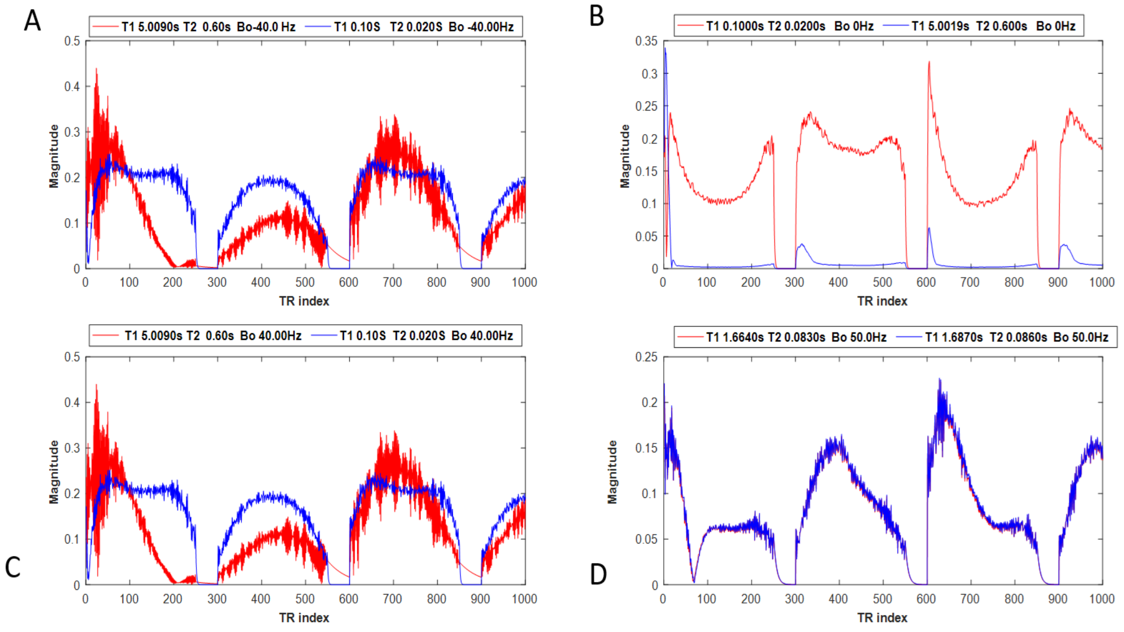

Figure 16: Dictionary entries. A), Comparison of dictionary entries with long and short T1, T2 along with positive off-resonance, B), dictionary entries with zero off-resonance or entries in resonance, C), Comparison of dictionary entries with long and short T1, T2 along with positive off-resonance, D), Comparison of dictionary entries with one dictionary step between each with same off-resonance values**.**

5.1.1. Simulation

The simulation was using the pulse sequence described in section 4.1.3 with spiral sampling techniques using the custom phantom and the brain phantom with spiral trajectory design as with 24 interleaves to fully sample the full image with 6 milliseconds to sample a single interleave using 5 microsecond sampling time. The first eight simulated images using a brain phantom with 6 interleaves and using a custom phantom with a single interleave are shown in Fig.17 and Fig. 18 respectively.

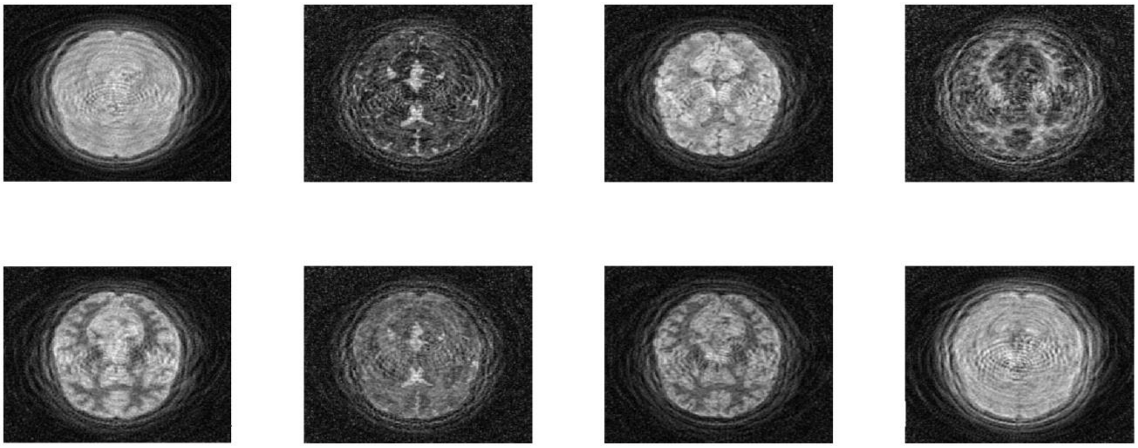

Figure 17: The first eight simulated images using a brain phantom with 6 interleave.

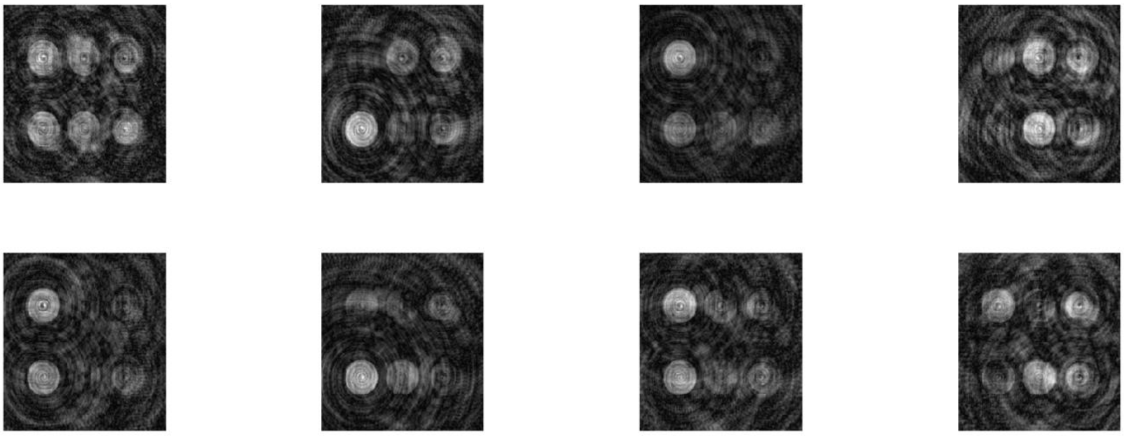

Figure 18: The first eight simulated images using a custom phantom with a single interleave.

The simulated image as shown in Fig 17 and Fig 18 was the output of the simulator framework using six interleave for simulated phantom and single interleave for custom phantom spiral undersampling. In fact, the simulated image has artifact affected but as we use pattern matching that will not affect the quantification procedure as a whole.

5.1.2. Custom Phantom Experiments

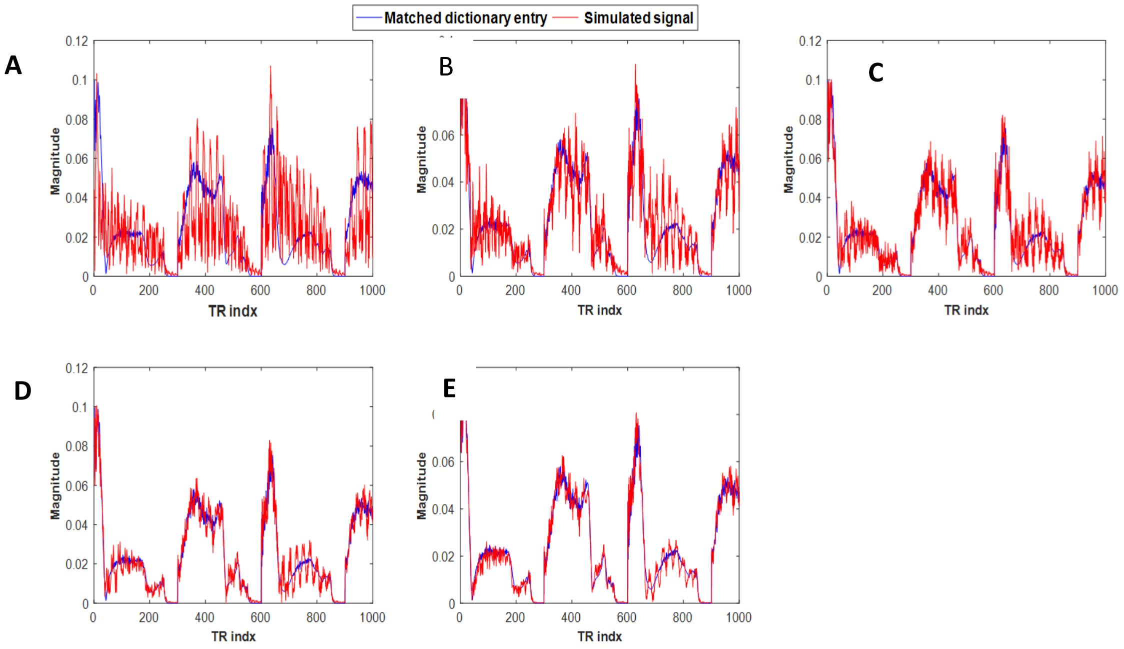

Figure 19: The signal curves of one voxel with T1 of 1250 ms, T2 of 496 ms, and 0 Hz off-resonance; their matched dictionary entries from a fully sampled data (E); and undersampled data at a rate (R) of 2 (D), 3 (C), 4 (B) and 24 (A). The plotted signals were normalized to the maximum of the sampled data.

It can be seen that the undersampled data is blurred and introduces aliasing artifacts in Fig. 17 and Fig. 18. Figures 19 illustrates the undersampling artifacts of a representative voxel intensity as a function of time, where the data is acquired with an MRF sequence based on balanced steady-state free precision (BSSFP) [5].

Figure 20 presents MRF matching results with images simulated using a custom generated phantom with ground truth for a different number of interleaves. The T1, T2, and off-resonance parameter values for the six ROIs in the phantom are listed in Table 2, Table 3, and Table 4. While Fig. 21, Fig. 22, and Fig. 23 depict a comparison of T1 relaxation, T2 relaxation, as well as off-resonance parameters of the MRF, matched results with a different number of spiral interleaves to the ground truth.

Map	**T1 in ROI 1 [s]**	**T1 in ROI 2 [s]**	**T1 in ROI 2 [s]**	**T1 in ROI 4 [s]**	**T1 in ROI 5 [s]**	**T1 in ROI 6 [s]**
Ground truth	5.012	1.545	0.811	0.53	1.425	1.425
R_1_Map	4.7974	1.5133	0.8443	0.5647	1.3737	1.3737
R_2_Map	4.8874	1.5155	0.8284	0.5725	1.3885	1.3885
R_3_Map	4.8393	1.51	0.8162	0.5794	1.3831	1.3831
R_4_Map	4.7922	1.5030	0.8074	0.5836	1.4064	1.4064
R_24_Map	4.9467	1.5312	0.8543	0.5588	1.4452	1.4452
R_1_Std	0.1461	0.0208	0.0173	0.01	0.0722	0.0722

R_2_Std	0.1539	0.0218	0.0167	0.012	0.0768	0.0768
R_3_Std	0.1619	0.025	0.0207	0.0105	0.0891	0.0891
R_4_Std	0.1621	0.0282	0.0224	0.0097	0.2100	0.2100
R_24_Std	0.122	0.0176	0.0254	0.0098	0.0828	0.0828

Table 2: T1 Relaxation parameter values in the six ROIs in the phantom.

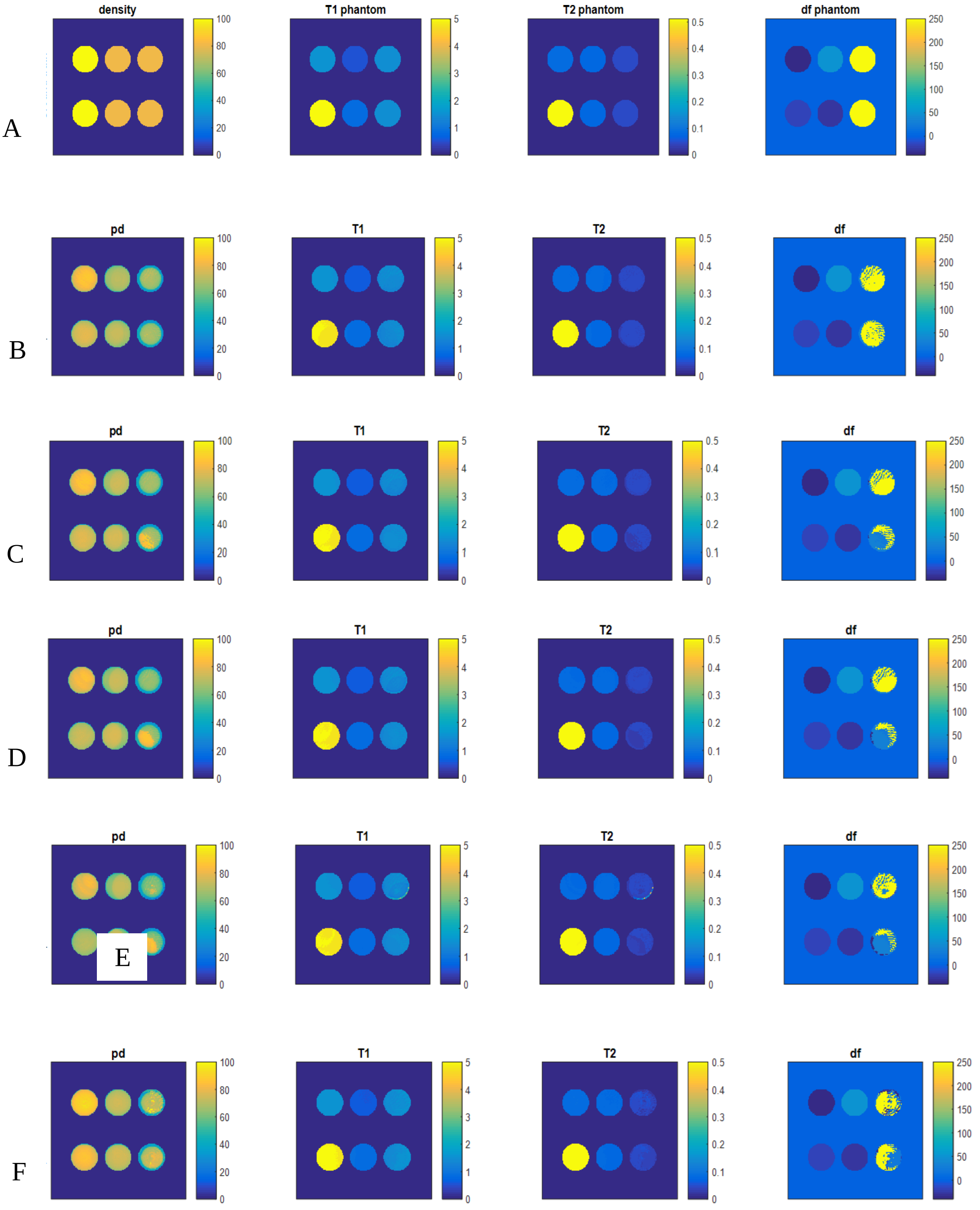

Figure 20: MRF matching results with images simulated using custom generated phantom with ground truth (A), Full sample 24 interleaves (b), 12 interleaves (C), 8 interleaves (D), 6 interleaves

(E), single interleaves (F). T1 map (s), T2 map (s), PD map, and df map (Hz) from left to right using 1000 time points.

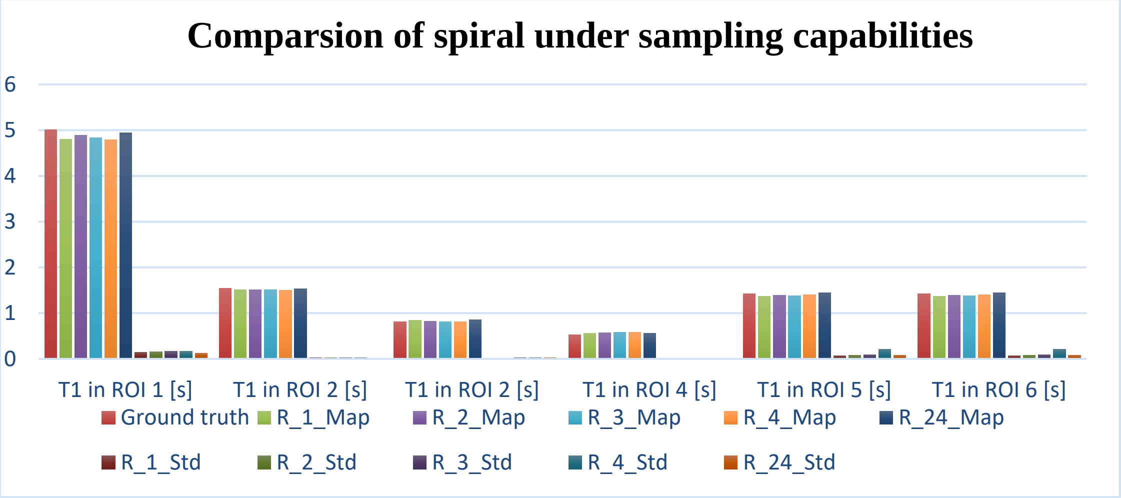

Figure 21: Comparison of T1 relaxation time of MRF matched result with a different number of spiral interleaves to the ground truth.

Map	**T2 in ROI 1 [s]**	**T2 in ROI 2 [s]**	**T2 in ROI 3 [s]**	**T2 in ROI 4 [s]**	**T2 in ROI 5 [s]**	**T2 in ROI 6 [s]**
Ground truth	0.512	0.083	0.077	0.077	0.041	0.041
R_1_ Map	0.510	0.0809	0.0783	0.0783	0.0415	0.0415
R_2_ Map	0.5044	0.0810	0.0780	0.0780	0.0390	0.0390
R_3_ Map	0.5047	0.0798	0.0777	0.0777	0.0381	0.0381
R_4_ Map	0.5047	0.078	0.0772	0.0772	0.0417	0.0417
R_24_ Map	0.5034	0.0829	0.0786	0.0786	0.0394	0.0394
R_1_ Std	0.0057	0.00150	0.0019	0.0019	0.0415	0.0415
R_2_ Std	0.0044	0.0016	0.002	0.002	0.0056	0.0056
R_3_ Std	0.0059	0.0021	0.0024	0.0024	0.0058	0.0058
R_4_ Std	0.0078	0.0027	0.0026	0.0026	0.0294	0.0294
R_24_ Std	0.0039	0.0011	0.0021	0.0021	0.0068	0.0068

Table 3: T2 Relaxation parameter values in the six ROIs in the phantom.

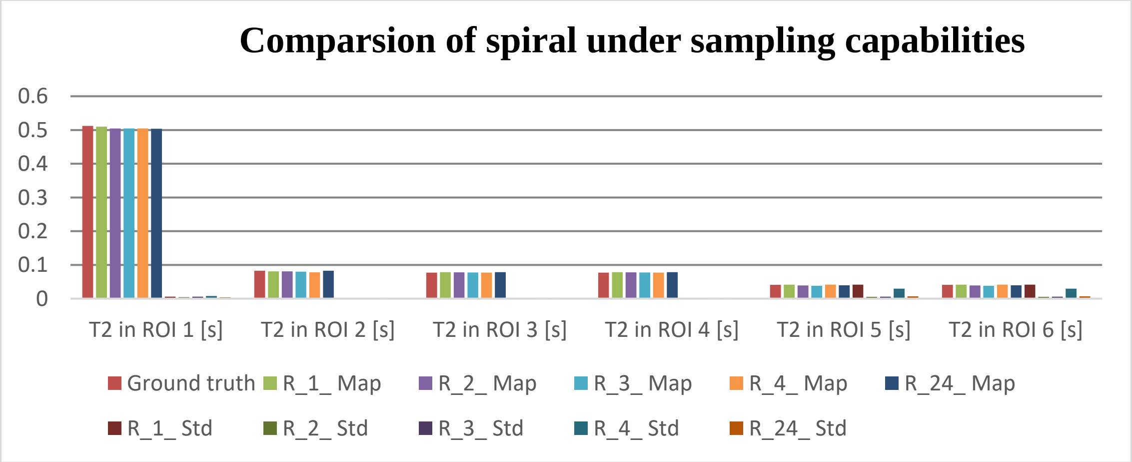

Figure 22: Comparison of T2 relaxation time of MRF matched result with a different number of spiral interleaves to the ground truth in the six regions of interest.

Map	**DF in ROI 1 [HZ]**	**DF in ROI 2 [HZ]**	**DF in ROI 3 [HZ]**	**DF in ROI 4 [HZ]**	**DF in ROI 5 [HZ]**	**DF in ROI 6 [HZ]**
Ground truth	-20	-40	-30	50	250	250
R_1_ Map	-20	-40	-30	50	196.7281	196.7281
R_2_ Map	-20	-40	-30	50	145.1008	145.1008
R_3_ Map	-20	-40	-30	50	133.0015	133.0015
R_4_ Map	-20	-40	-30	50	119.7736	119.7736
R_24_ Map	-20	-40	-30	50	148.3604	148.3604
R_1_ Std	0	0	0	0	96.2827	96.2827
R_2_ Std	0	0	0	0	112.565	112.565
R_3_ Std	0	0	0	0	111.7693	111.7693
R_4_ Std	0	0	0	0	109.7736	109.7736
R_24_ Std	0	0	0	0	112.5861	112.5861

Table 4: Off-resonance parameter values in the six ROIs in the phantom.

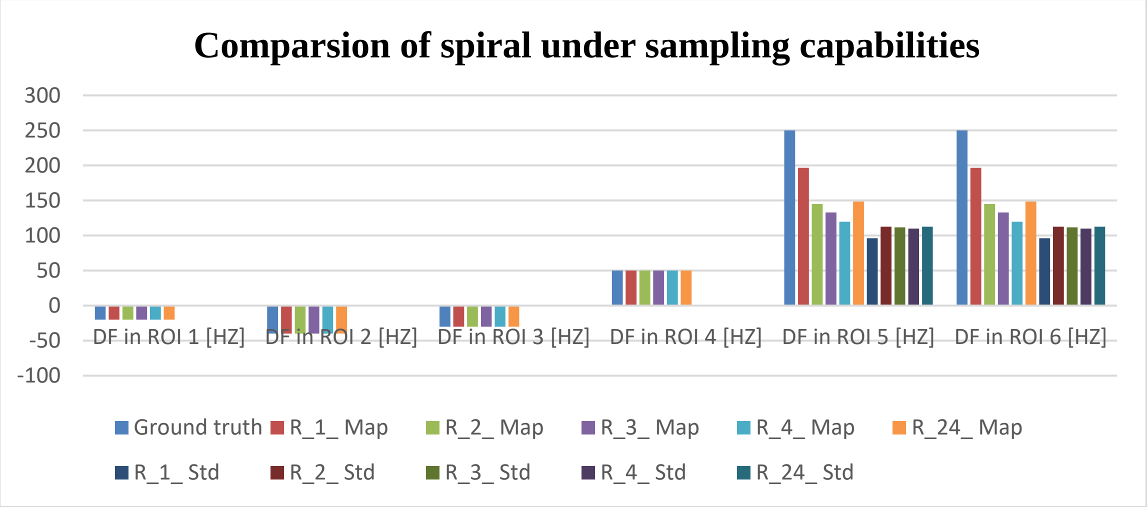

Figure 23: Comparison of off-resonance of MRF matched result with a different number of spiral interleaves to the ground truth in the six regions of interest.

The above Figures show the quantified T1, T2, PD, and off-resonance frequency values from the custom phantom experiment, which are well within the acceptable range. As it can be seen in charts, the T1, T2, and off-resonance values were compared with those from the ground truth values within the selected region of interest for different undersampling levels. Undersampling at level 24 has an acceptable result with less time which will accelerate the MRF parameter mapping procedure. The mean T1 and T2 values generated from the custom phantom experiment from each region listed in the above Tables are in good agreement with the ground truth values and similarly the off-resonance value except at the border or with high values that have some deviation.

5.1.3. Brain Phantom Experiments

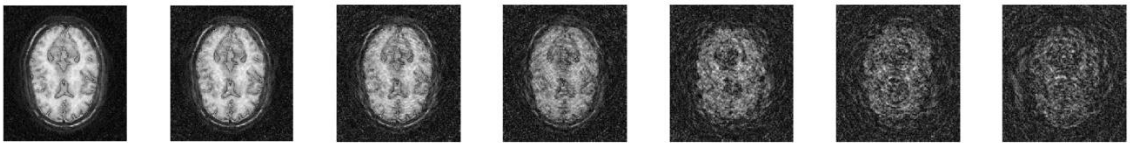

Figure 24: Simulated image at serious 111 of TR index using MRF simulator with full (24), 12, 8, 6, 4, 2, single interleave without additive noise respectively.

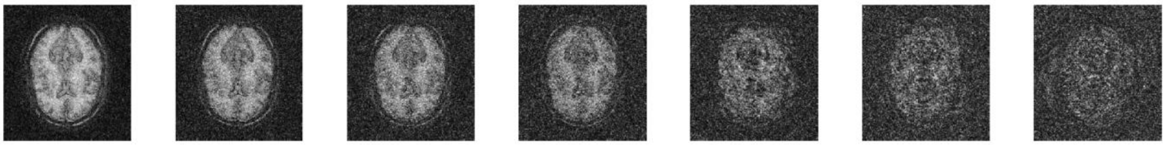

Figure 25: Simulated image at serious 111 of TR index using MRF simulator with full (24), 12, 8, 6, 4, 2, single interleave with additive noise respectively.

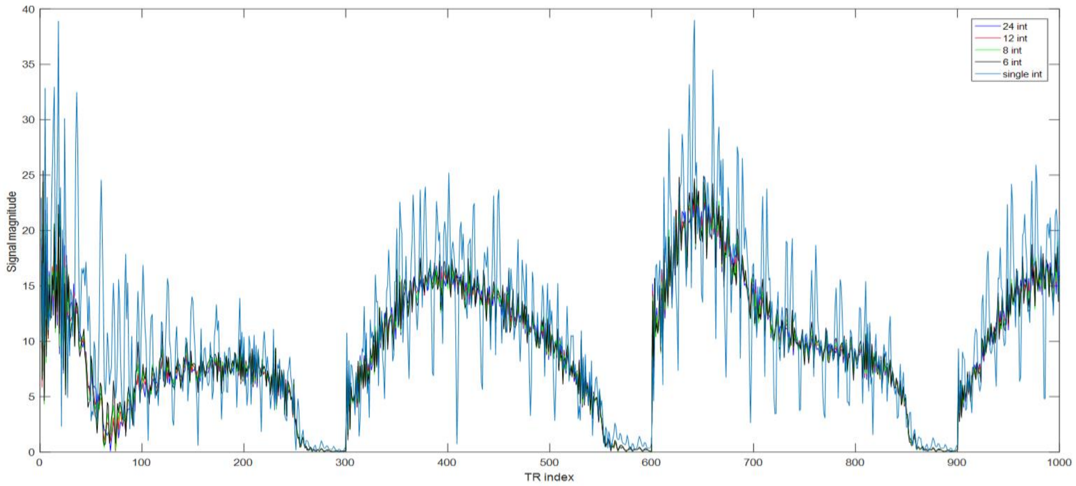

Figure 26: Signal evolution of original simulated signal with full sample (24) interleaves,12 interleaves, 8 interleaves, 6 interleaves, and single-shot (interleaves) blue, red, green, black, and cyan color respectively.

Figure 24 and Fig. 25 present simulated brain images for a different number of interleaves (full (24), 12, 8, 6, and single-shot) without and with additive noise, respectively. The corresponding signal evolution curves are shown in Fig. 26. The MRF matched results (T1, T2, and off-resonance) for a different number of spiral interleaves are depicted in Fig. 27. The T1, T2, and off-resonance parameter mean values and standard deviation for the six brain phantom slices are listed in Table 5, Table 6, and Table 7. While Fig. 28, Fig. 28, and Fig. 30 depict a comparison of T1 relaxation, T2 relaxation, as well as off-resonance parameters of the MRF, matched results with a different number of spiral interleaves to the ground truth.

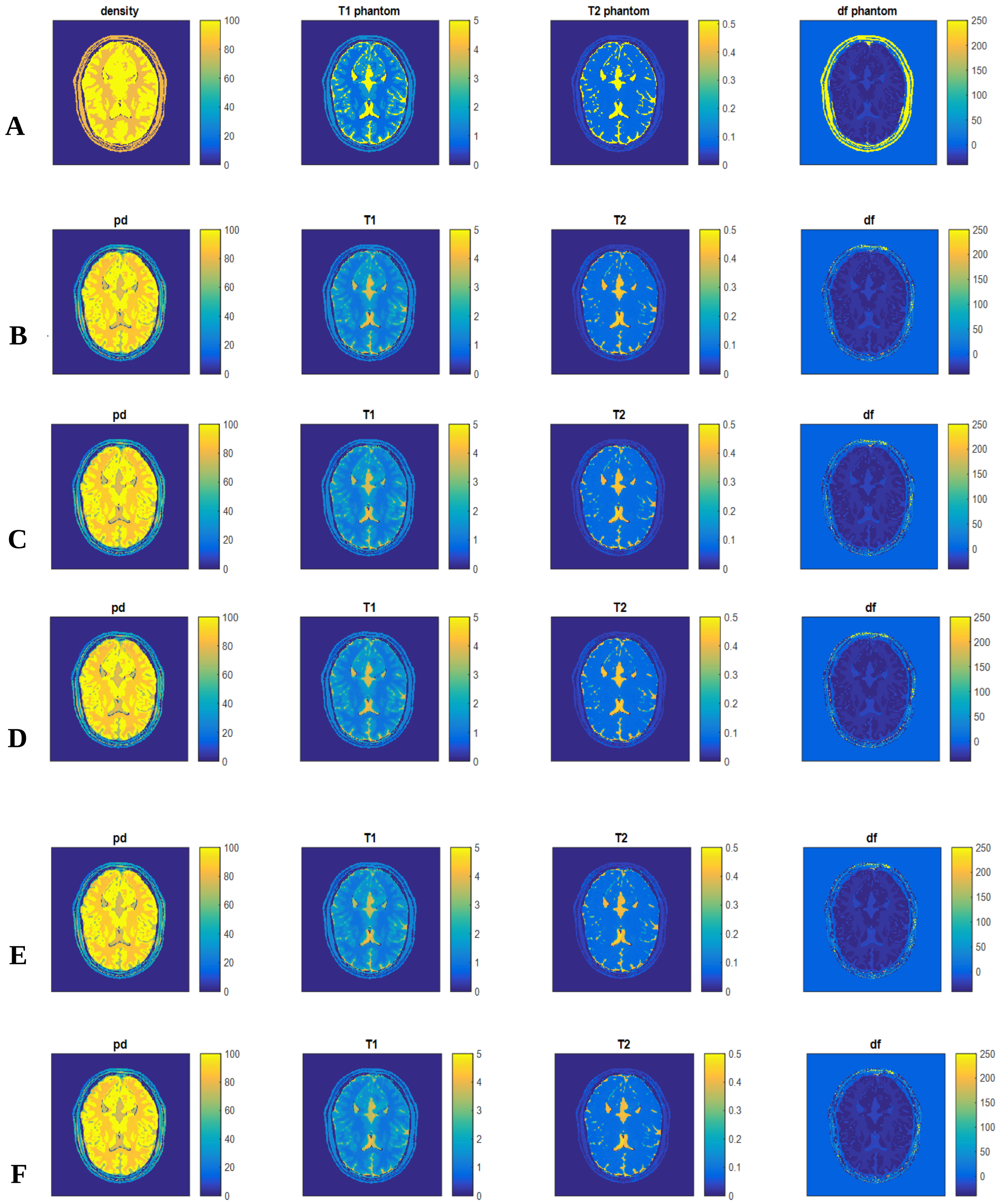

Figure 27: MRF matching results with images simulated using brain phantom with ground truth (A), Full sample 24 interleaves (b), 12 interleaves (C), 8 interleaves (D), 6 interleaves (E), single interleaves (F). T1 map (s), T2 map (s), PD map, and df map (Hz) from left to right using 1000 time points.

Relaxation parameter and off-resonance values in the six ROIs using brain phantom**.**

Map	**T1 in ROI 1 [s]**	**T1 in ROI 2 [s]**	**T1 in ROI 2 [s]**	**T1 in ROI 4 [s]**	**T1 in ROI 5 [s]**	**T1 in ROI 6 [s]**
Ground truth	5.012	1.545	0.811	0.53	1.425	1.425
R_1_Map	3.0554	1.5664	1.0818	0.8241	1.3321	1.3321
R_2_Map	3.0622	1.568	1.080	0.8279	1.339	1.339
R_3_Map	2.9917	1.564	1.0935	0.8358	1.338	1.338
R_4_Map	2.92	1.561	1.107	0.847	1.338	1.338
R_24_Map	3.207	1.578	1.0549	0.8162	1.363	1.363
R_1_Std	0.785	0.2597	0.1273	0.1469	0.3261	0.3261
R_2_Std	0.7976	0.2664	0.133	0.147	0.326	0.326
R_3_Std	0.7624	0.260	0.140	0.147	0.309	0.309
R_4_Std	0.7766	0.261	0.1351	0.1466	0.3158	0.315
R_24_Std	0.8412	0.286	0.1354	0.1571	0.3491	0.3491

Table 5: T1 Relaxation parameter values in the six ROIs in the phantom.

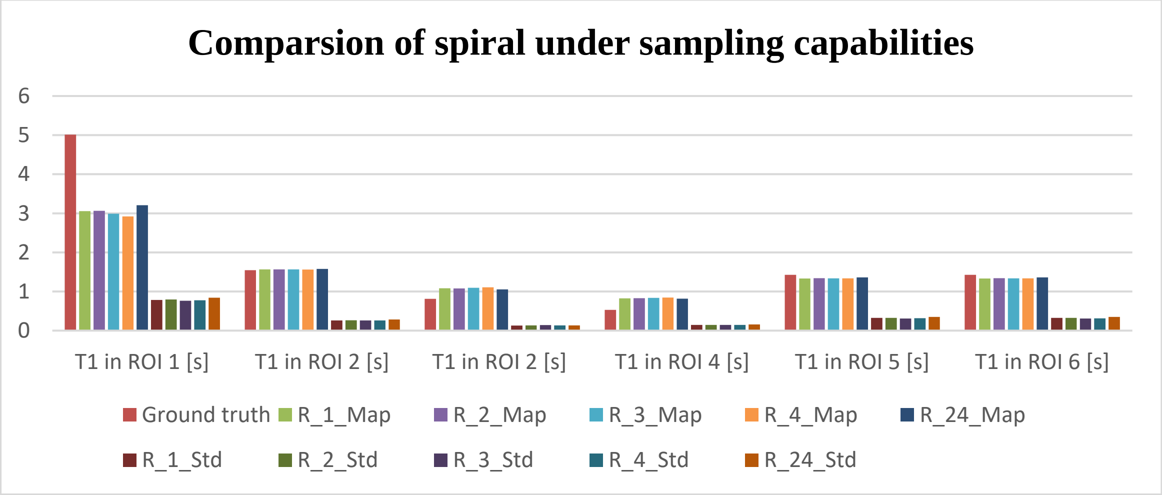

Figure 28: Comparison of T1 relaxation time of MRF matched result with a different number of spiral interleaves to the ground truth in the six regions of interest.

Map	**T2 in ROI 1 [s]**	**T2 in ROI 2 [s]**	**T2 in ROI 3 [s]**	**T2 in ROI 4 [s]**	**T2 in ROI 5 [s]**	**T2 in ROI 6 [s]**
Ground truth	0.512	0.083	0.077	0.077	0.041	0.041
R_1_ Map	0.3269	0.090	0.0812	0.0812	0.04989	0.04989
R_2_ Map	0.3265	0.090	0.0811	0.0811	0.0492	0.0492
R_3_ Map	0.3175	0.091	0.0815	0.0815	0.049	0.049
R_4_ Map	0.3096	0.0911	0.0819	0.0819	0.049	0.049
R_24_ Map	0.3388	0.0913	0.0803	0.0803	0.0555	0.0555
R_1_ Std	0.1288	0.0358	0.0134	0.0134	0.0489	0.0489
R_2_ Std	0.129	0.036	0.013	0.013	0.049	0.049
R_3_ Std	0.129	0.036	0.0137	0.0137	0.0487	0.0487
R_4_ Std	0.1296	0.0360	0.0137	0.0137	0.0466	0.0466
R_24_ Std	0.1327	0.0387	0.01578	0.0157	0.0539	0.0539

Table 6: T2 Relaxation parameter values in the six ROIs in the phantom.

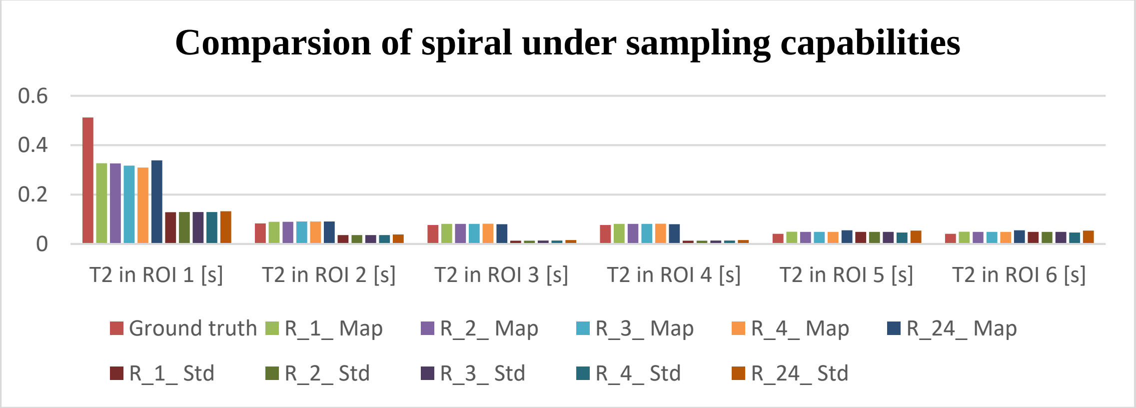

Figure 29: Comparison of T2 relaxation time of MRF matched result with a different number of spiral interleaves to the ground truth in the six regions of interest.

Map	DF in ROI 1 [HZ]	DF in ROI 2 [HZ]	DF in ROI 3 [HZ]	DF in ROI 4 [HZ]	DF in ROI 5 [HZ]	DF in ROI 6 [HZ]
Ground truth	-20	-40	-30	50	250	250
R_1_ Map	-22.66	-38.438	-30.40	44.697	49.164	49.164
R_2_ Map	-22.71	-38.46	-30.369	44.58	50.119	50.119
R_3_ Map	-22.856	-38.43	-30.38	44.23	47.748	47.748
R_4_ Map	-23.101	-38.41	-30.34	43.846	46.256	46.256
R_24_ Map	-22.457	-37.29	-28.43	43.269	51.48	51.48
R_1_ Std	6.7885	5.557	5.99	10.7	49.348	49.348
R_2_ Std	6.837	5.379	6.207	10.83	51.86	51.86
R_3_ Std	7.129	5.40	6.27	7.72	48.457	48.457
R_4_ Std	7.365	5.385	6.549	11.135	45.895	45.895
R_24_ Std	7.79	10.99	13.05	8.2	58.56	58.56

Table 7: Off-resonance parameter values in the six ROIs in the phantom.

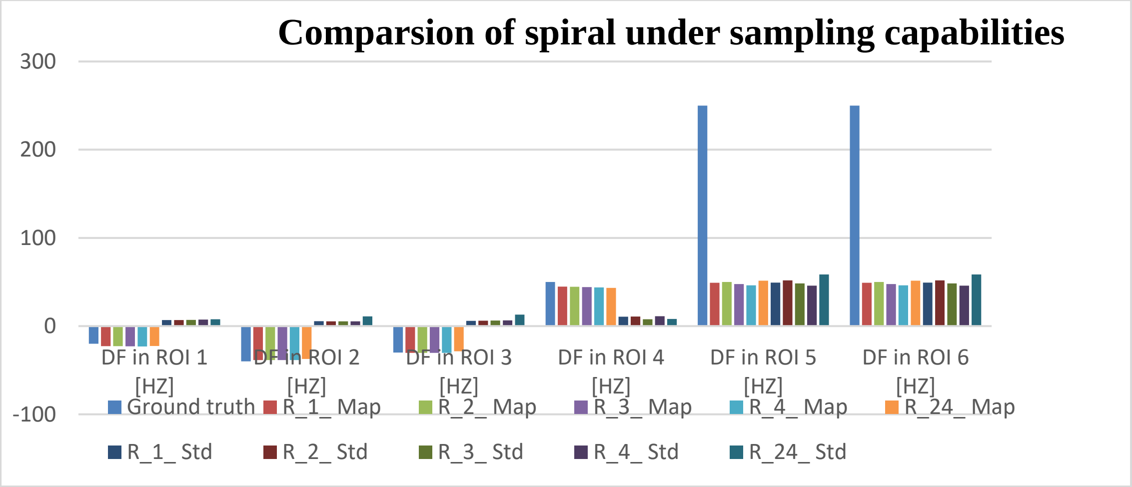

Figure 30: Comparison of off-resonance of MRF matched result with a different number of spiral interleaves to the ground truth in the six regions of interest.

The above Figures show the quantified T1, T2, PD, and off-resonance frequency values from the brain phantom experiment, which are well within the acceptable range. As it can be seen in charts, the T1, T2, and off-resonance values were compared with those from the ground truth values within the selected region of interest for different undersampling levels. Undersampling at level 24 has an acceptable result with less time which will accelerate the MRF parameter mapping procedure. The mean T1 and T2 values generated from the brain phantom experiment from each region listed in the above Tables are in good agreement with the ground truth values and similarly the off-resonance value except at the border or with high values that have many deviations.

5.1.4. Evaluating Undersampling Capability of MRF

Here the undersampling capability of MRF using both custom generated phantoms and brain phantoms was evaluated by generating the parameter map using different under sampling levels (1, 2, 3, 4, and 24) shown in Fig. 20 and Fig. 27. The results for the custom phantoms are the ones shown in Fig. 21, 22, and 23 as well as Tables 2, 3, and 4. The results for that of the brain phantoms are the ones shown in Fig. 28, 29, and 30 as well as Tables 5, 6, and 7. The two sets of results show that the undersampling at level 24 has the acceptable values of T1, T2, and DF across all six regions of interest (ROI) by comparing the values to the ground truth.

5.1.5. Effect of Noise on the Parameter Map

Here the effect of noise that is added to the real and imaginary parts of the simulated signal with different levels is evaluated by comparing the parameter maps of the resulting noisy signals against the ground truth. Figures 31, 32, and 33 present some of the results. The figures clearly show that the parameter maps depend on the level of noise added and the undersampling level. The higher the noise level the higher the effect on the parameter map. Also, the more we under-sample, the more the effect of noise appears on the parameter map. Generally speaking, the effect of noise is more pronounced on the off-resonance maps than the other parameters.

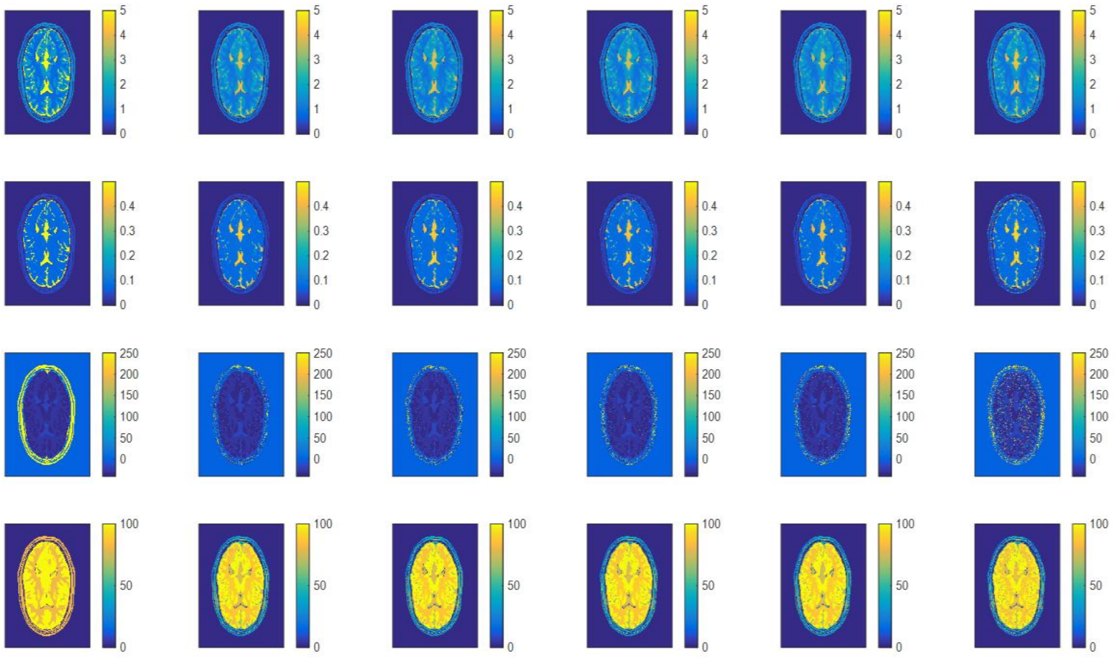

Figure 31: MRF matching results with ground truth, full sample, 12 interleaves, 8 interleaves, 6 interleaves, and single interleave (column) with T1, T2, DF, and PD map (row) with noise level 1.

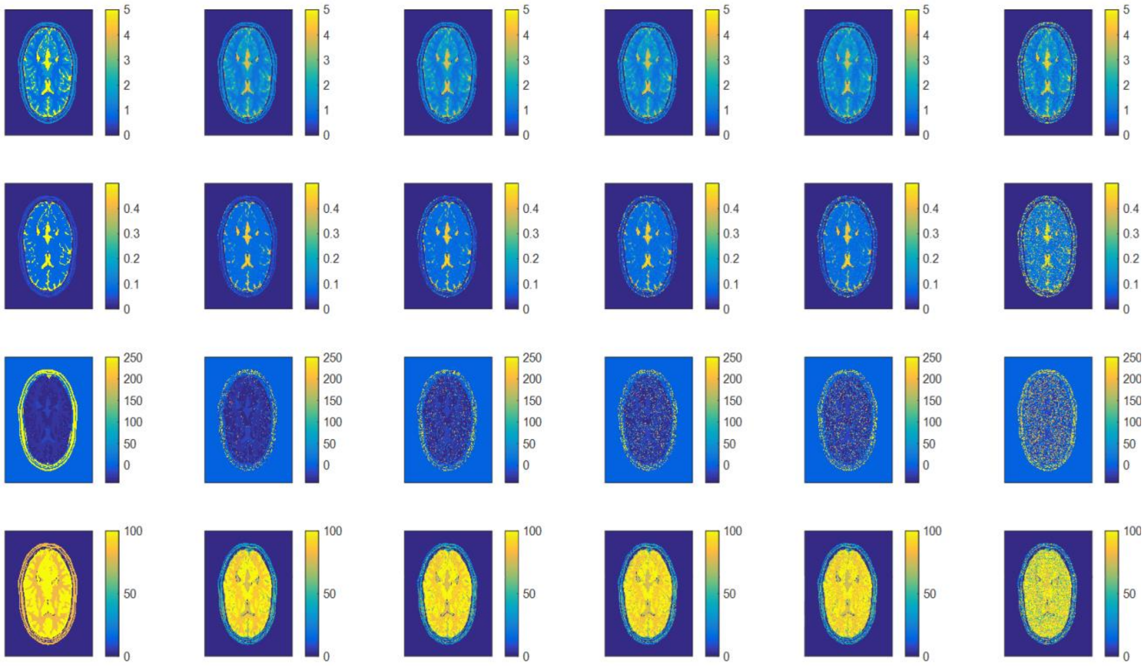

Figure 32: MRF matching results with ground truth, full sample, 12 interleaves, 8 interleaves, 6 interleaves, and single interleave (column) with T1, T2, DF, and PD map (row) with noise level 2.

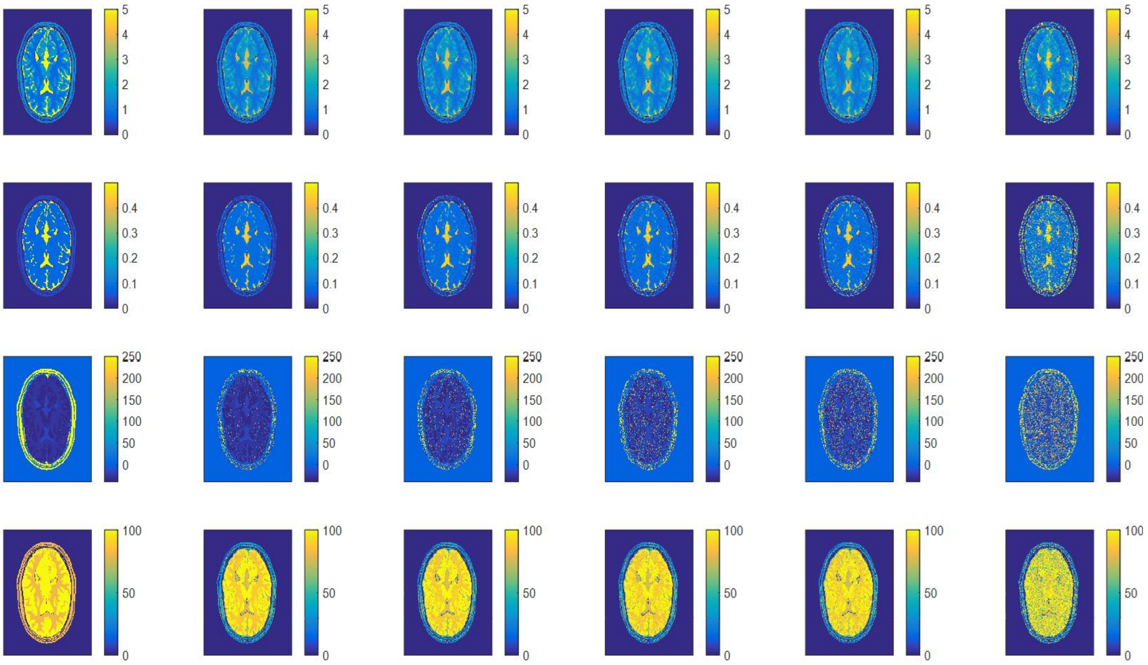

Figure 33: MRF matching results with ground truth, full sample, 12 interleaves, 8 interleaves, 6 interleaves, and single interleave (column) with T1, T2, DF, and PD map (row) with noise level 3**.**

5.1.6. Simulation Comparison

Simulation comparison between the existing and the newly proposed method was performed using the undersampled parameter map with the factor of 24 using brain phantoms. The results are summarized in Figures 34 to 43 and Tables 8 to 13. The signal evolution curves for the proposed and existing simulation using six and single spiral interleave are shown respectively in Fig. 34 and Fig. 35. The MRF matched results (T1, T2, and off-resonance) for single spiral interleave with and without additive noise are depicted in Fig. 36 and Fig. 37 respectively. The T1, T2, and off-resonance parameter mean values and standard deviation for the six brain phantom slices are listed in Tables 8 to 13. While Figures 38 to 43 depict a comparison of T1 relaxation, T2 relaxation, as well as off-resonance parameters of the MRF, matched results using single spiral interleave to the ground truth with and without additive noise.

The comparison between the existing versus proposed simulation and the gradient effect which really happens in the real scanning is simulated in the proposed simulation which indeed makes the proposed simulation more complete than the existing simulation type for MRF.

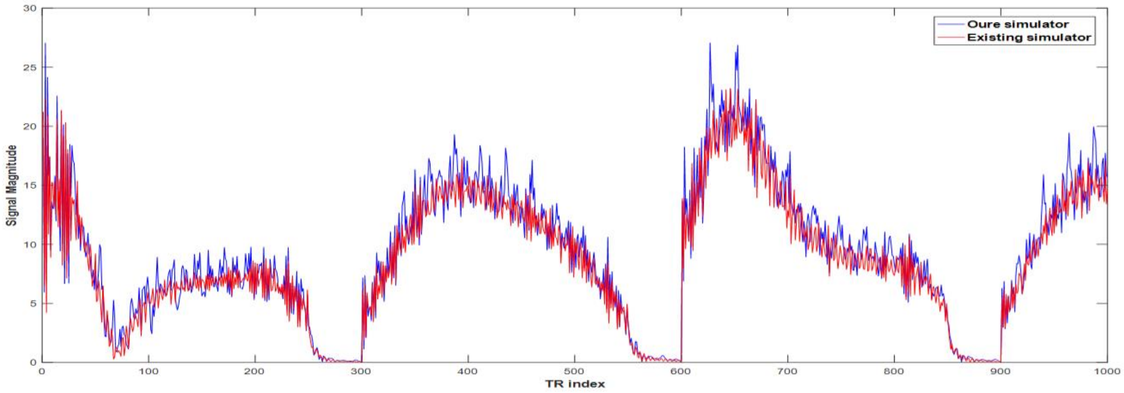

Figure 34: Simulated signal evolution with existing vs proposed MRF simulator using 6 interleave spiral sampling.

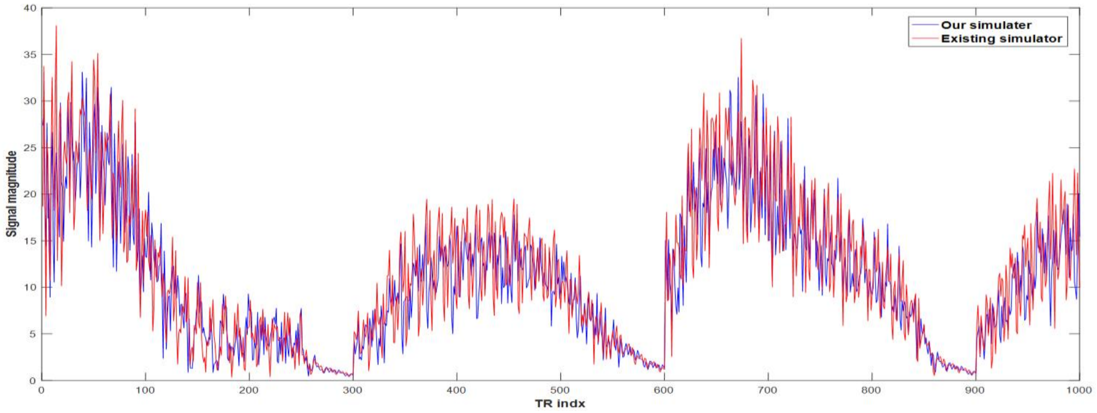

Figure 35: Simulated signal evolution with existing vs proposed MRF simulator using single interleave spiral sampling.

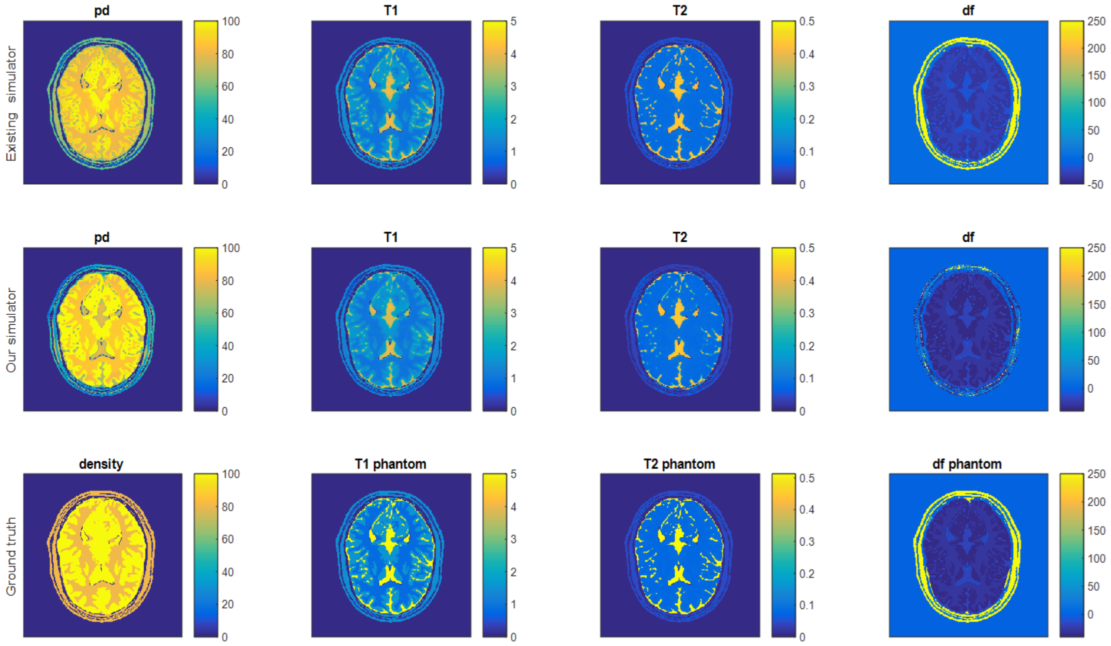

Figure 36: MRF matching results with images simulated using the existing simulator and the proposed MRF simulator with a single interleave without additive noise and ground truth. T1 map (s), T2 map (s), PD map, and Bo map (Hz) from left to right using 1000 time points.

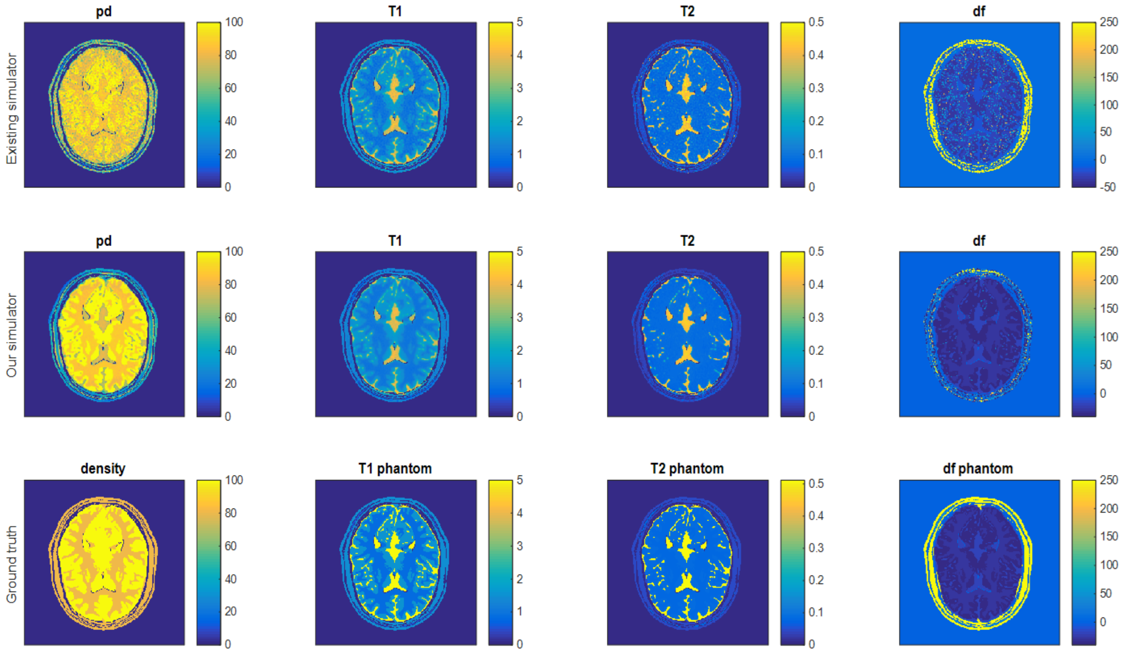

Figure 37: MRF matching results with images simulated using the existing simulator and the proposed MRF simulator with a single interleave with additive noise and ground truth. T1 map (s), T2 map (s), PD map, and Bo map (Hz) from left to right using 1000 time points.

As it shown in Fig 36 and 37 the noise more pronounced on the map generated from the existing simulator specially on the off-resonance map of the existing simulation than the proposed simulation.

Map	**T1 in ROI 1 [s]**	**T1 in ROI 2 [s]**	**T1 in ROI 2 [s]**	**T1 in ROI 4 [s]**	**T1 in ROI 5 [s]**	**T1 in ROI 6 [s]**
Ground truth	5.012	1.545	0.811	0.53	1.425	1.425
R_24_Map_Exsiting	3.483	1.636	1.046	0.414	1.463	1.463
R_24_Map_Our	3.207	1.578	1.0549	0.8162	1.363	1.363
R_24_Std_Exsiting	0.5363	0.283	0.0986	0.8745	0.2171	0.2171
R_24_Std_Our	0.8412	0.286	0.1354	0.1571	0.3491	0.3491

Table 8: T1 Relaxation parameter values in the six ROIs in the phantom.

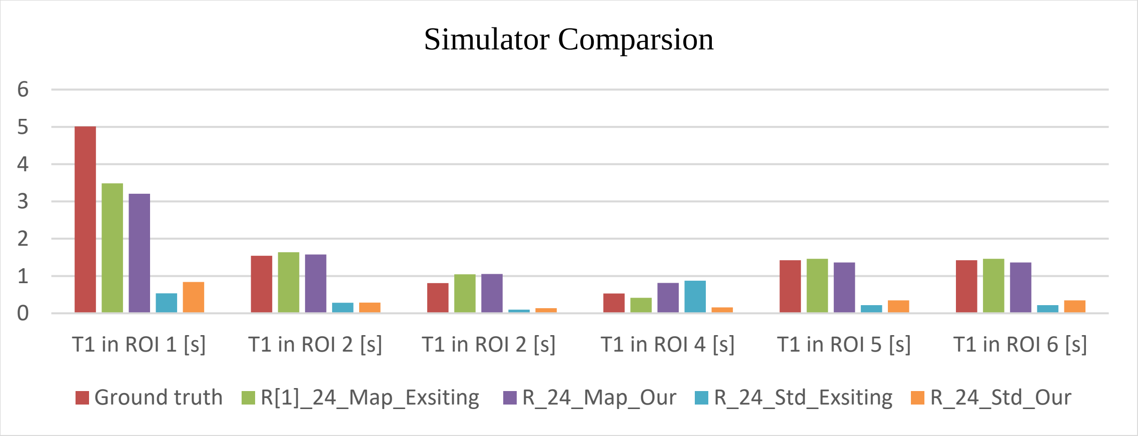

Figure 38: Comparison of T1 relaxation times of MRF matched results using the proposed simulator, existing simulator, and the ground truth in the six regions of interest.

Map	**T1 in ROI 1 [s]**	**T1 in ROI 2 [s]**	**T1 in ROI 2 [s]**	**T1 in ROI 4 [s]**	**T1 in ROI 5 [s]**	**T1 in ROI 6 [s]**
Ground truth	5.012	1.545	0.811	0.53	1.425	1.425
R_24_N_Map_Exsiting	3.485	1.6419	1.0509	0.4739	1.525	1.525
R_24_ N_Map_Our	3.2169	1.5815	1.0585	0.8173	1.3991	1.3991
R_24_ N_Std_Exsiting	0.5639	0.311	0.138	0.9581	0.372	0.3725
R_24_ N_Std_Our	0.8642	0.311	0.160	0.1989	0.574	0.574

Table 9: Noisy T1 Relaxation parameter values in the six ROIs in the phantom.

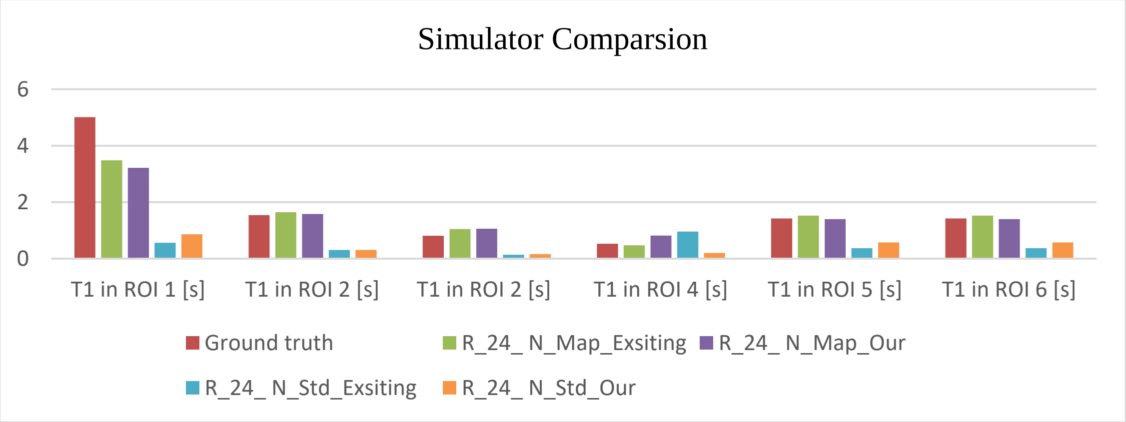

Figure 39: Comparison of noise added T1 relaxation times of MRF matched results using the proposed simulator, existing simulator, and the ground truth in the six regions of interest.

Map	**T2 in ROI 1 [s]**	**T2 in ROI 2 [s]**	**T2 in ROI 3 [s]**	**T2 in ROI 4 [s]**	**T2 in ROI 5 [s]**	**T2 in ROI 6 [s]**
Ground truth	0.512	0.083	0.077	0.077	0.041	0.041
R_24_ Map _Existing	0.398	0.094	0.083	0.083	0.0523	0.0523
R_24_ Map_Our	0.3388	0.0913	0.0803	0.0803	0.0555	0.0555
R_24_ Std_Existing	0.064	0.0302	0.0164	0.0164	0.0190	0.0190
R_24_ Std_Our	0.1327	0.0387	0.01578	0.0157	0.0539	0.0539

Table 10: T2 Relaxation parameter values in the six ROIs in the phantom.

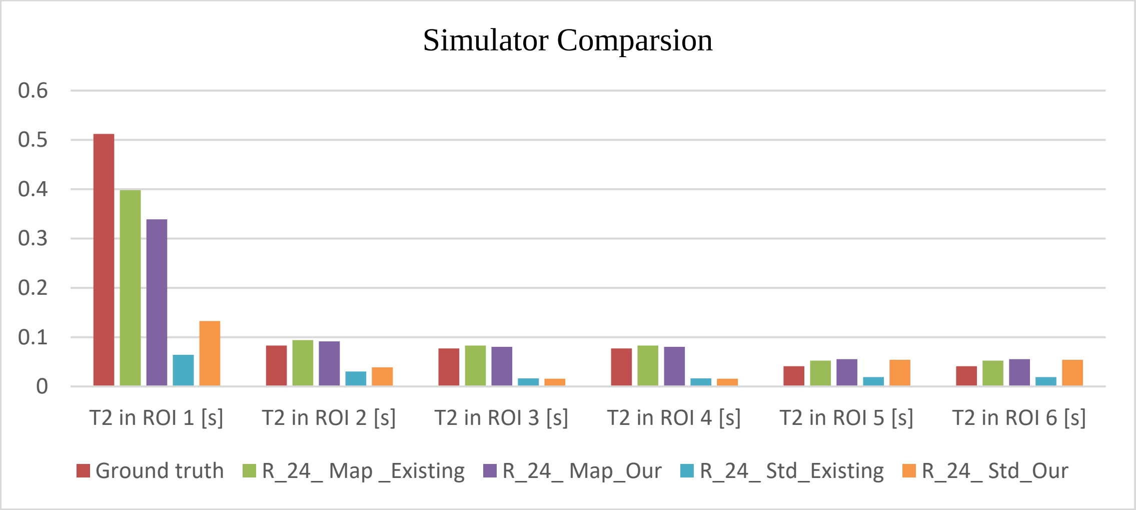

Figure 40: Comparison of T2 relaxation times of MRF matched results using the proposed simulator, existing simulator, and the ground truth in the six regions of interest.

Map	**T2 in ROI 1 [s]**	**T2 in ROI 2 [s]**	**T2 in ROI 3 [s]**	**T2 in ROI 4 [s]**	**T2 in ROI 5 [s]**	**T2 in ROI 6 [s]**
Ground truth	0.512	0.083	0.077	0.077	0.041	0.041
R_24_ N_Map _Existing	0.395	0.098	0.0883	0.0883	0.05995	0.0599
R_24_ N_Map_Our	0.3345	0.094	0.08167	0.08167	0.0912	0.0912
R_24_ N_Std_Existing	0.0828	0.0398	0.0310	0.0310	0.0426	0.0426
R_24_ N_ Std_Our	0.1416	0.041	0.0190	0.0190	0.108	0.108

Table 11: Noisy T2 Relaxation parameter values in the six ROIs in the phantom.

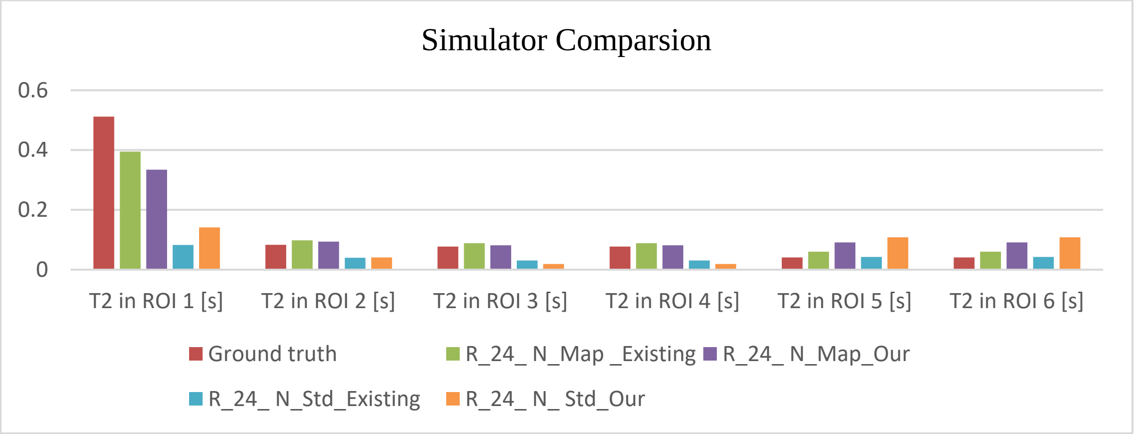

Figure 41: Comparison of noise added T2 relaxation times of MRF matched results using the proposed simulator, existing simulator, and the ground truth in the six regions of interest.

Map	**DF in ROI 1 [HZ]**	**DF in ROI 2 [HZ]**	**DF in ROI 3 [HZ]**	**DF in ROI 4 [HZ]**	**DF in ROI 5 [HZ]**	**DF in ROI 6 [HZ]**
Ground truth	-20	-40	-30	50	250	250
R_24_ Map_Existing	-20.282	-38.777	-30.313	51.95	228.773	228.773
R_24_ Map_our	-22.457	-37.29	-28.43	43.269	51.48	51.48
R_24_ Std_Existing	2.622	4.979	3.542	25.04	65.414	65.41
R_24_ Std_Our	7.79	10.99	13.05	8.2	58.56	58.56

Table 12: Off-resonance parameter map values in the six ROIs in the phantom.

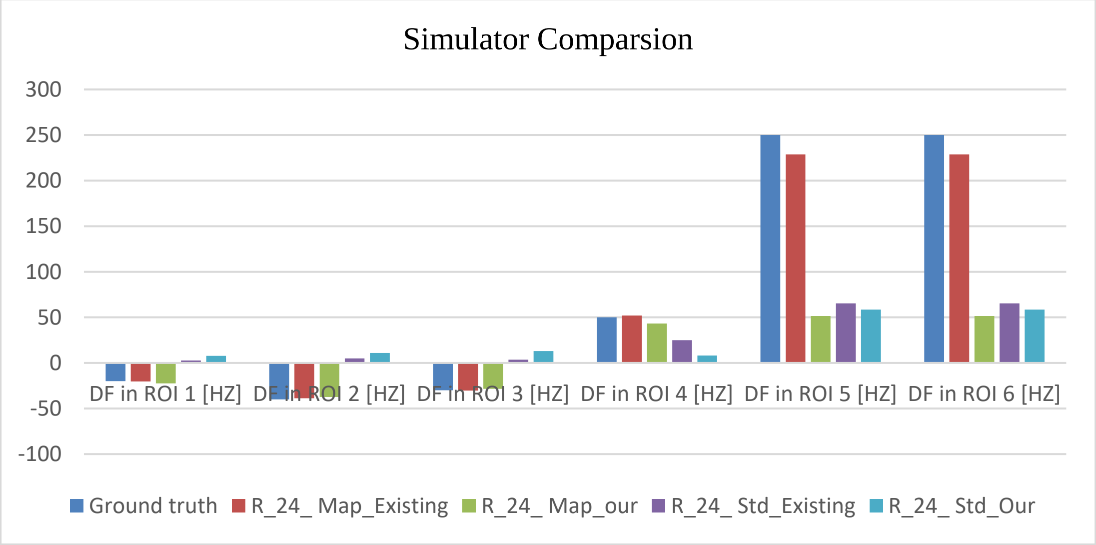

Figure 42: Comparison of off-resonance of MRF matched results using the proposed simulator, existing simulator, and the ground truth in the six regions of interest.

Map	**DF in ROI 1 [HZ]**	**DF in ROI 2 [HZ]**	**DF in ROI 3 [HZ]**	**DF in ROI 4 [HZ]**	**DF in ROI 5 [HZ]**	**DF in ROI 6 [HZ]**
Ground truth	-20	-40	-30	50	250	250
R_24_ N_Map_Existing	-19.62	-27.16	-13.82	67.293	177.250	177.250
R_24_N_ Map_our	-14.72	-20.1	-12.78	52.82	89.887	89.887
R_24_ N_Std_Existing	10.153	35.94	38.332	68.374	103.408	103.408
R_24_N_ Std_Our	34.72	50.18	46.51	48.258	92.899	92.899

Table 13: Noisy off-resonance parameter map values in the six ROIs in the phantom.

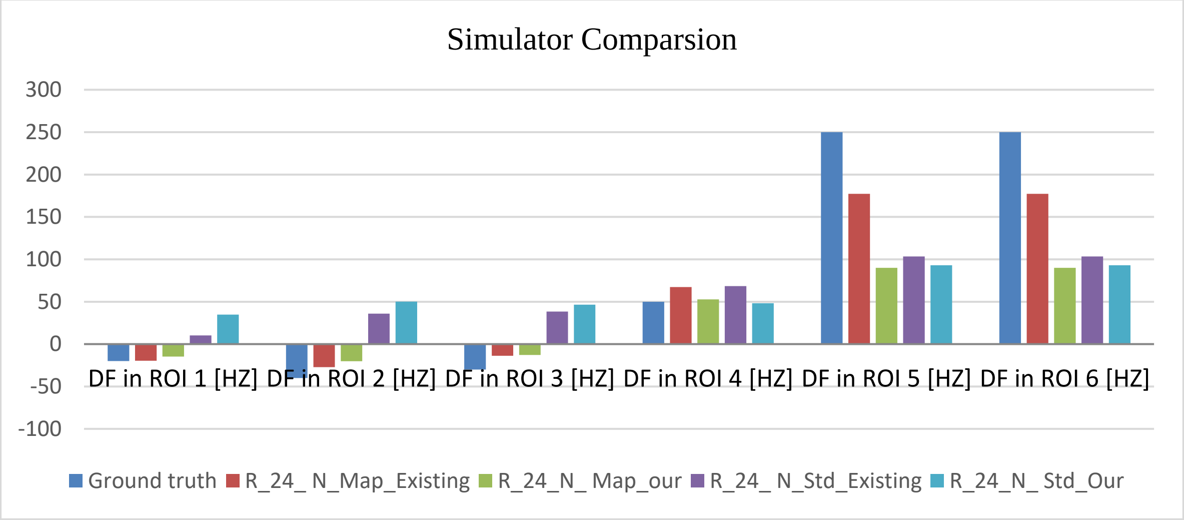

Figure 43: Comparison of noise added off-resonance of MRF matched results using the proposed simulator, existing simulator, and the ground truth in the six regions of interest.

5.2. Discussion

As the acceleration or undersampling rate increases, the value of the inner product (pattern matching) decreases because of the more undersampling artifact. Irrespective of the undersampling artifacts, the predicted values of T1, T2, and DF are still very close as it is clearly seen in the results presented in Section 5.1. As far as we used the direct image reconstruction method using the NUFFT toolbox, it is expected that the image will have the effect of the reconstruction due to gridding and interpolation which is mainly seen on the full sample images. In fact, it affects the accuracy of the quantification of the parameter maps in the later stage when the matching process is done.

As the undersampling level during simulation increases, the effects of noise on the parameter maps became more visible. As the undersampling level decreases, the effects of noise became less visible even on the off-resonance maps. This clearly shows the relationship between the undersampling level and the effect of noise on the parameter maps. At a given undersampling level, as the level of noise increases, its effect on the parameter maps gets more and more pronounced.

In the simulation comparison, more interesting was the effect of the sampling gradient during the image acquisition step. This makes the proposed simulation more complete than existing simulations. Existing simulation techniques assume the effect of sampling gradient is negligible. As it is seen on the parameter maps on the results presented in the previous section, the effect of the sampling gradient is significant particularly on the off-resonance maps.

Chapter 6 : Conclusion and Future Works

6.1. Conclusion

In this thesis, we have presented a principal simulation framework for MRF using the spiral sampling technique and proved the feasibility of an MRF sequence with IR_BSSFP spiral readout for rapid quantification of T1, T2, DF, and density of the specific tissue with the severely undersampled spiral sampling. The basis for the simulation was the technique proposed on the original MRF paper [5]. The key parts of the approach have been: representation of the signal model through Bloch simulation; sampling using analytical variable density spiral sampling; evaluating undersampling capability; evaluating the effects of noise on the parameter maps and comparing the simulation framework with existing simulation method.

6.2. Future Works

- It might be very important to use some deep learning techniques to accelerate the MRF parameter mapping process. There are some promising results in MRF that make use of deep learning which will improve and reduce the time it takes for the matching, dictionary generation, and simulation.

- Also, implementing the simulation framework on a GPU platform should make the simulation much faster than just a CPU.

- The entire experiment should be repeated on synthetic phantoms using in vivo data in order to verify the effectiveness of the proposed MRF technique.

- Instead of the direct image reconstruction approach adopted in this thesis, the use of iterative image reconstruction approaches could improve the accuracy of the parameter maps.

Appendix

Appendix A: Basic MATLAB Code for simulation

```
clc
clear
close all
clear path
addpath Dictionary_genration
addpath Bloch_simulation
addpath Gradiant_genration
addpath Sequence_design
addpath Phantom_genration/Brain_phantom;
addpath Phantom_genration/Custom_phantom;
%% User defined settings:
% phantomString = 'brain';
% phantomString= 'custom';
phantomString = 'brain';


%% setting sequence parameters
Num_TRs=1000;
RFpulses=generate_RF(Num_TRs);
TR=generate_TR(Num_TRs);
N_inter=24; % number of interleaves
FOV=30; % cm same FOV of phantom and recon
NumPixX=256; % phantom size and recon size
NumPixY=256;
ResFactor=1;  % To increase simulation spatial resolution
Time_Sim_Factor=1; % To increase simulation temporal resolution
res=FOV/NumPixX; % Phantom's spatial resolution
sim_res=res/ResFactor;  % simulation spatial resolution
```

```
[k_space,g,time] = spiral_interleaved(N_inter,3,FOV,NumPixX);
%%Generate the  gradient
Sampling_Time_Steps=size(k_space,1);
G_Samp_Time=time(end)-time(end-1);
[kr,gr] = rewinder(k_space,g,time,G_Samp_Time); %% rewind
[all_gradient_values, all_k_values] =
generate_all_trajectories3(gr,kr,N_inter,'step7');%rotate the
spiral
%% generate phantom
switch (phantomString)
case 'brain'
[ density, T1_phantom, T2_phantom, df_phantom ] = Brain_phantom1;
case 'custom'
[ density,T1_phantom,T2_phantom, df_phantom ] =
generate_phantoms(256);
end

density1=zeros(NumPixX*ResFactor,NumPixY*ResFactor);
T1_phantom1=zeros(NumPixX*ResFactor,NumPixY*ResFactor);
T2_phantom1=zeros(NumPixX*ResFactor,NumPixY*ResFactor);
df_phantom1=zeros(NumPixX*ResFactor,NumPixY*ResFactor);

for mm=1:ResFactor
    for nn=1:ResFactor
        density1(mm:ResFactor:end,nn:ResFactor:end)=density;
        T1_phantom1(mm:ResFactor:end,nn:ResFactor:end)=T1_phantom;
        T2_phantom1(mm:ResFactor:end,nn:ResFactor:end)=T2_phantom;
        df_phantom1(mm:ResFactor:end,nn:ResFactor:end)=df_phantom;

    end
end

%% sampling using discrete Bloch simulation
tic
```

```
rf=abs(RFpulses);
rph=angle(RFpulses);
L = length(TR);
s = numel(all_gradient_values.rep2(:,1));
% all_samples1 = zeros(Sampling_Time_Steps,L,3);
all_samples = zeros(s,L);
for j=1:24 % looping over the interleaves
     j

if j==1
    A=all_gradient_values.rep1;
elseif j==2
    A=all_gradient_values.rep2;
elseif j==3
    A=all_gradient_values.rep3;
% end
elseif j==4
    A=all_gradient_values.rep4;
elseif j==5
    A=all_gradient_values.rep5;
elseif j==6
    A=all_gradient_values.rep6;
elseif j==7
    A=all_gradient_values.rep7;
% end
elseif j==8
    A=all_gradient_values.rep8;
 elseif j==9
    A=all_gradient_values.rep9;
    elseif j==10
    A=all_gradient_values.rep10;
elseif j==11
    A=all_gradient_values.rep11;
% end
```

```
elseif j==12
    A=all_gradient_values.rep12;
 elseif j==14
    A=all_gradient_values.rep14;
    elseif j==15
    A=all_gradient_values.rep15;
elseif j==16
    A=all_gradient_values.rep16;
% end
elseif j==17
    A=all_gradient_values.rep17;
 elseif j==19
    A=all_gradient_values.rep19;
    elseif j==20
    A=all_gradient_values.rep20;
elseif j==21
    A=all_gradient_values.rep21;
% end
elseif j==22
    A=all_gradient_values.rep22;
 elseif j==23
    A=all_gradient_values.rep23;
else
    A=all_gradient_values.rep24;
end
M = zeros(NumPixX*ResFactor,NumPixY*ResFactor,3);
M(:,:,3) =  -density1;
Nx = size(M,1);
Ny = size(M,2);
M = (reshape(M,Nx*Ny,3)).';
beta = zeros(Nx,Ny);
for i=1:1000 % % looping over the number of TRs
     i
```

```
    [M , all_samples(:,i)]=
Bloc_Main(M,A(:,i),rf(i),rph(i),G_Samp_Time,T1_phantom1,T2_phantom1
,density1,df_phantom1,Nx,ResFactor,sim_res,Time_Sim_Factor);

rem_time = TR(i)- G_Samp_Time*s; %after gradient time till next RF
pulse

   beta = df_phantom1.* rem_time*2*pi;
    M = rotation_z(M,beta);

M=relax(M,rem_time,T1_phantom1,T2_phantom1,density1,NumPixY*ResFact
or); %
    all_samples1(:,:,j)=all_samples(1:Sampling_Time_Steps,:);
end
end

toc



  %% Save Raw Data
save -v7.3 ./Spiral1194_Ts5us_TR1000_Rot15_Inter24.mat
all_gradient_values all_k_values all_samples1

%% reconstruction
%it needs NUFFT tool box
addpath 'irt-clone-master';setup;

%% single spiral
tic
k_1_int_noised_full_signal=zeros(256,256,1000);
for i=1:1000
      k_1_int=[all_k_values.rep1(1:1194,i) ];
      k_1_int_kspace=all_samples1(:,i,1);
      k_1_int_kspace=permute(k_1_int_kspace,[1 3 2]);
```

```
[noised_kspace]=Add_noise(k_1_int_kspace,density,sd_level);

[image1]=ITRATIVE_NUFFT(noised_kspace,k_1_int);
%
k_1_int_noised_full_signal(:,:,i)=image1;


end

toc
signal_n =k_1_int_noised_full_signal;

%% dictionary generation
disp('genrate the dictionary...');
[dict, dict_norm, lut] = dict_true(RFpulses,TR);
%% pattern Matching

disp('matching...');
[~,~,~,T1_map,T2_map,pd_map,df_map]=fast_matching(dict,signal_n,lut
,T1_phantom,T2_phantom,density,df_phantom,dict_norm);
```

Appendix B: Basic MATLAB Code for simulation comparison

```
clc
clear
close all
addpath Phantom_genration/Brain_phantom;
addpath Phantom_genration/Custom_phantom;
addpath Gradiant_genration
addpath Sequance_design
addpath Dictionary_genration
load sequence
%generate phantoms
[ density, T1_phantom, T2_phantom, df_phantom,phantom] =
Brain_phantom1(RFpulses, TR);

% generate spiral
N_inter=24;
[k_space,g,time] = spiral_interleaved(N_inter,3,30,256);



[all_gradient_values, all_k_values] =
generate_all_trajectories3(g,k_space,N_inter,'step1');%rotate the
spiral

%% generating undersampled image using NUFFT toolbox
addpath 'irt-clone-master';setup;

signal=zeros(256,256,1000);
parfor i=1:1000
%%six interleaves spiral undersampling
k_6_int=[all_k_values.rep1(1:1194,i) all_k_values.rep5(1:1194,i)
all_k_values.rep9(1:1194,i)  all_k_values.rep13(1:1194,i)
all_k_values.rep17(1:1194,i)  all_k_values.rep21(1:1194,i) ];
kspace=k_6_int(:);
kspace = [real(kspace(:)) imag(kspace(:))];
```

```
[ samples_data]=Forward(phantom(:,:,i),kspace); % compute the
forward to reconstruct the image

wi = col(l2_norm(kspace,2)); % simple density compensation

[ image ] = Adjoint( kspace,samples_data,wi(:),256);%compute the
adjoint to reconstruct the image

signal(:,:,i)=image;


end
%%


disp('genrate the dictionary...');
     [dict, dict_norm, lut] = dict_true(RFpulses,TR);


disp('matching...');
[~,~,~,T1,T2,pd,df] =
fast_matching(dict,signal,lut,T1_phantom,T2_phantom,density,df_phan
tom,dict_norm);
```

References

[1] M. A. Bernstein, K. F. King and X. J .Zhou, Handbook Of MRI Pulse Sequences, San Diego, California: Elsevier Academic Press, 2004.

[2] R.W. Brown, Y. N. Cheng, E. M. Haacke, M. R. Thompson and R. Venkatesan, Magnetic Resonance Imaging:Physical Principles and Sequence Design, NewJersey Hoboken: JohnWiley&Sons, 2014.

[3] P. Tofts, Quantitative MRI of the brain: measuring changes caused by disease, England: JohnWiley & Sons, 2005.

[4] S. C. Deoni, "Quantitative relaxometry of the brain," *Top Magn Reson Imaging,* vol. 21, no. 2, pp. 101-113, 2010.

[5] D. Ma, V. Gulani, N. Seiberlich, K. Liu, J. L. Sunshine, J. L. Duerk and M. A.Griswold, "Magnetic resonance fingerprinting," *Nature,* vol. 495, no. 7440, pp. 187-192, 2013.

[6] D. Rundle, S. Kishore, S. Seshadri, and F. Wehrli, "Magnetic Resonance Imaging Simulator:A Teaching Tool for Radiology," *Journal of Digital Imaging,* vol. 3, no. 4, pp. 226-229, 1990.

[7] G. Torheim, P. A. Rinck, R. A. Jones, and J.Kvaerness, "A simulator for teaching MR image contrast behavior," *MAGMA* , vol. 2, pp. 515-522, 1994.

[8] F.Bloch, "Nuclear induction," *phsical review,* vol. 70, pp. 461-471, 1946.

[9] S.Ljunggren, "A simple graphical representation of fourier-based imaging methods," *Journal of Magnetic Resonance,* p. 383–43, 1983.

[10] G. H. Glover and J. M.Pauly, "Projection reconstruction technique for reduction of motion effects in MRI.," *Magnetic Resonance in Medicine* , pp. 275-289, 1992.

[11] K. Scheffler and J.Hennig, "Reduced Circular Field-of-View Imaging," *Magnetic Resonance in Medicine,* vol. 40, pp. 474-480, 1998.

[12] D. Kim, E. Adalsteinsson, and D. M. Spielman., "Simple analytic variable density spiral design," *Magn Reson Med,* pp. 214-219, 2003.

[13] G. Glover, "Simple analytic spiral k-space algorithm," *Magn Reson Med,* pp. 412-415, 1999.

[14] K. F. King, T. K. Foo, and C. R. Crawford., "Optimized gradient waveforms for spiral scanning.," *Magnetic Resonance in Medicine,* vol. 34, pp. 156-160, 1995.

[15] J. H Lee,B. A. Hargreaves,B. S. Hu, and D. G. Nishimura, "Fast 3D Imaging Using Variable-Density Spiral Trajectories With Applications to Limb Perfusion," *Magnetic Resonance in*

Medicine, vol. 50, p. 1276–1285 , 2003.

[16] C. H. Meyer, B. S. Hu, D. G. Nishimura,and A. Macovski, "Fast spiral coronary artery imaging," *Magnetic Resonances in Medicine* , vol. 28, pp. 202-213, 1992.

[17] J. A. Fessler and B. P.Sutton, "Nonuniform fast Fourier transforms using min_max interpolation.," *IEEE Transactions on Signal Processing,* vol. 51, pp. 560 - 574, 2003.

[18] R.D. Hoge, R. K. S. Kwan, G. B. Pike, "Density Compensation Functions for Spiral MRI," *Magnetic Resonance in medicine ,* vol. 38, pp. 117-128, 1997.

[19] P.J.Beatty, D. G. Nishimura , J. M. Pauly , "Rapid gridding reconstruction with a minimal oversampling ratio.," *IEEE Transactions On Medical Imaging* , vol. 24, no. 6, pp. 799-808, 2005.

[20] V. Rasche, R. Proksa ,R. Sinkus , P. Brnert ,H. Eggers , " Resampling of data between arbitrary grids using convolution interpolation," *IEEE Transactions On Medical Imaging ,* vol. 18, no. 5, pp. 385-392, 1999.

[21] W. Li, M. Griswold, and X Yu, "Rapid T1 Mapping of Mouse Myocardium With Saturation Recovery Look-Locker Method," *Magnetic Resonance in Medicine,* vol. 64, p. 1296–1303 , 2010.

[22] D.C. Look, D.R. Locker, "Time Saving in Measurement of NMR and EPR Relaxation Times," *The Review Of Scientific Instruments* , vol. 41, no. 2, pp. 250-251, 1970.

[23] S. C.L. Deoni, B. K. Rutt, and T. M. Peters, "Rapid Combined T1 and T2 Mapping Using Gradient Recalled Acquisition in the Steady State," *Magnetic Resonance in Medicine,* vol. 49, pp. 515-526, 2003.

[24] J. Homer and M. S. Reever, "Driven-Equilibrium Single-Pulse Observation of T1, Relaxation. A Reevaluation of a Rapid “New” Method for Determining NMR Spin-Lattice Relaxation Times," *Journal of magnetic resonance* , vol. 63, pp. 287-297, 1985.

[25] E.K.Farm, R.J. Herfkens, G.A. Jonson, G.H. Glover,J.P.Karis, A.Shimakawa,T.G.Perkins,and N.J.Pact, "Rapid Calculation Of Tl Using Variable Flip Angle Gradient Refocused Imaging," *magnetic resonance imaging,* vol. 5, pp. 201-208, 1987.

[26] P. Ehses,N. Seiberlich,D. Ma, F. A. Breuer, P. M. Jakob,M. A. Griswold, and V. Gulani, "IR TrueFISP With a Golden-Ratio-Based Radial Readout:Fast Quantification of T1, T2, and Proton Density," *Magnetic Resonance in Medicine* , vol. 69, pp. 71-81, 2013.

[27] P. Schmitt, M. A. Griswold, P. M. Jakob, M. Kotas, V. Gulani,M. Flentje, and A. Haase, "Inversion Recovery TrueFISP: Quantification of T1, T2,and spin density," *Magnetic Resonance in Medicine,* vol. 51, pp. 661-667, 2004.

[28] V. Gulani, P. Schmitt, M. A. Griswold, A. G. Webb,and P. M. Jakob, "Towards a single-sequence neurologic magnetic resonance imaging examination:multiple-contrast images from an IR TrueFISP experiment.," *Investigative Radiology ,* vol. 39, pp. 767-774, 2004.

[29] Y.Jiang, D.Ma, N.Seiberlich,V. Gulani ,M.A. Griswold, "MR fingerprinting using fast imaging with steady state precession (FISP) with spiral readout," *Magnetic Resonance in Medicine,* vol. 74, no. 6, pp. 1621-1631, 2015.

[30] Y.Jiang, D.Ma ,R. Jerecic ,J. Duerk , N.Seiberlich ,V. Gulani ,M.A. Griswold, "MR fingerprinting using the quick echo splitting NMR imaging technique," *Magnetic Resonance in Medicine,* vol. 77, no. 3, pp. 979-988, 2017.

[31] K. S. Nayak, B. A. Hargreaves, B. S. Hu, D. G. Nishimura, J. M. Pauly, and C. H. Meyer, "Spiral Balanced Steady-State Free Precession Cardiac Imaging," *Magnetic Resonance in Medicine,* vol. 53, p. 1468–1473, 2005.

[32] C. J. Hardy and H. E. Cline, "Broadband nuclear magnetic resonance pulses with two-dimensional spatial selectivity," *Journal of Applied Physics,* 1989.

[33] "BrainWeb: Simulated Brain Database," [Online]. Available: https://brainweb.bic.mni.mcgill.ca/brainweb/. [Accessed 7 October 2019].

[34] D.L. Collins, A.P. Zijdenbos, V. Kollokian, J.G. Sled, N.J. Kabani, C.J. Holmes, A.C. Evans , "Design and Construction of a Realistic Digital Brain Phantom," *IEEE Transactions on Medical Imaging,* vol. 17, no. 3, pp. 463-468, 1998.

[35] M. Davies and G. Puy and P. Vandergheynst and Y. Wiaux, "A compressed sensing framework for magnetic resonance fingerprinting," 2014. [Online]. Available: https://arxiv.org/abs/1312.2465v2.

[36] M. Golbabaeey, Z. Chenx z , Y. Wiauxx , and M. Davies, "CoverBLIP: accelerated and scalable iterative matched-filtering for Magnetic Resonance Fingerprint reconstruction," 2018. [Online]. Available: https://arxiv.org/abs/1810.01967v1.

[37] "Michigan Image Reconstruction Toolbox (MIRT)," [Online]. Available: http://web.eecs.umich.edu/~fessler/irt/fessler.tgz..

[38] W. A. Edelstein, G. H. Glover, C . J. Hardy, and R. W. Redington , "The Intrinsic Signal-to-Noise Ratio in NMR Imaging," *Magnetic Resonance in Medicine ,* vol. 3, pp. 604-618, 1986.

[39] Z. Wanga, D. Cuib, J. Zhangc, E. X. Wu, E. S. Hui, "MRF-ZOOM for the unbalanced steady-state free precession (ubSSFP)," *Magnetic Resonance Imaging,* vol. 65, pp. 146-154, 2020.

[40] Z. Wang , J. Zhang, D. Cui , J. Xie, M. Lyu, E. S. Hui , and E. X. Wu, "Magnetic resonance fingerprinting using a fast dictionary searching algorithm: MRF-ZOOM," *IEEE*

TRANSACTIONS ON BIOMEDICAL ENGINEERING, vol. 66, no. 6, pp. 1526-1535, 2019.

[41] Z. Wang, "MRF-ZOOM: A fast dictionary searching algorithm for magnetic resonance fingerprinting," 2015. [Online]. Available: arXiv:1506.05393.

[42] J. Assländer, M. A. Cloos, F. Knoll, D. K. Sodickson, J. Hennig, and R. Lattanzi, "Low Rank Alternating Direction Method of Multipliers Reconstruction for MR Fingerprinting," *Magnatic Resonance in Medicine* , vol. 79, no. 1, p. 83–96, 2018.

[43] G. Mazora, L. Weizman, A. Tal, and Y. C. Eldar, "Low Rank Magnetic Resonance Fingerprinting," 2018.